OPTICAL MONITORING OF THE BROAD-LINE RADIO GALAXY 3C 390.3[*]

Matthias Dietrich[1], Bradley M. Peterson[1], Catherine J. Grier[1], Misty C. Bentz[1,2], Jason Eastman[1,3],
Stephan Frank[1,4], Raymond Gonzalez[1], Jennifer L. Marshall[1,5], Darren L. DePoy[1,5,6], and Jose L. Prieto[1,7]

[1] Department of Astronomy, The Ohio State University, 140 West 18th Avenue, Columbus, OH 43210, USA; dietrich@astronomy.ohio-state.edu
[2] Department of Physics and Astronomy, Georgia State University, One Park Place South, Suite 700, Atlanta, GA 30303, USA
[3] Department of Physics, University of California, Broida Hall, Santa Barbara, CA 93 106, USA
[4] Laboratoire d'Astrophysique de Marseille/LAM Observatoire Astronomique de Marseille-Provence,
Pole de l'Etoile Site de Chateau-Gombert 38, rue Frederic Joliot-Curie, 13388 Marseille Cedex 13, France
[5] Department of Physics and Astronomy, Texas A&M University, 4242 TAMU, College Station, TX 77843, USA
[6] George P. and Cynthia Woods Mitchell Institute for Fundamental Physics and Astronomy, Texas A&M University, 4242 TAMU, College Station, TX 77843, USA
[7] Observatories of the Carnegie Institute of Washington, 813 Santa Barbara Street, Pasadena, CA 91101, USA

ABSTRACT

We have undertaken a new ground-based monitoring campaign on the broad-line radio galaxy 3C 390.3 to improve the measurement of the size of the broad emission-line region and to estimate the black hole mass. Optical spectra and g-band images were observed in late 2005 for three months using the 2.4 m telescope at MDM Observatory. Integrated emission-line flux variations were measured for the hydrogen Balmer lines Hα, Hβ, Hγ, and for the helium line He $\text{II}\lambda4686$, as well as g-band fluxes and the optical active galactic nucleus (AGN) continuum at $\lambda = 5100$ Å. The g-band fluxes and the optical AGN continuum vary simultaneously within the uncertainties, $\tau_{\text{cent}} = (0.2 \pm 1.1)$ days. We find that the emission-line variations are delayed with respect to the variable g-band continuum by $\tau(\text{H}\alpha) = 56.3^{+2.4}_{-6.6}$ days, $\tau(\text{H}\beta) = 44.3^{+3.0}_{-3.3}$ days, $\tau(\text{H}\gamma) = 58.1^{+4.3}_{-6.1}$ days, and $\tau(\text{He II } 4686) = 22.3^{+6.5}_{-3.8}$ days. The blue and red peaks in the double-peaked line profiles, as well as the blue and red outer profile wings, vary simultaneously within ± 3 days. This provides strong support for gravitationally bound orbital motion of the dominant part of the line-emitting gas. Combining the time delay of the strong Balmer emission lines of Hα and Hβ and the separation of the blue and red peaks in the broad double-peaked profiles in their rms spectra, we determine $M_{bh}^{\text{vir}} = 1.77^{+0.29}_{-0.31} \times 10^8 \, M_\odot$ and using σ_{line} of the rms spectra $M_{bh}^{\text{vir}} = 2.60^{+0.23}_{-0.31} \times 10^8 \, M_\odot$ for the central black hole of 3C 390.3, respectively. Using the inclination angle of the line-emitting region which is measured from superluminal motion detected in the radio range, accretion disk models to fit the optical double-peaked emission-line profiles, and X-ray observations, the mass of the black hole amounts to $M_{\text{bh}} = 0.86^{+0.19}_{-0.18} \times 10^9 \, M_\odot$ (peak separation) and $M_{\text{bh}} = 1.26^{+0.21}_{-0.16} \times 10^9 \, M_\odot$ (σ_{line}), respectively. This result is consistent with the black hole masses indicated by simple accretion disk models to describe the observed double-peaked profiles, derived from the stellar dynamics of 3C 390.3, and with the AGN radius–luminosity relation. Thus, 3C 390.3 as a radio-loud AGN with a low Eddington ratio, $L_{\text{edd}}/L_{\text{bol}} = 0.02$, follows the same AGN radius–luminosity relation as radio-quiet AGNs.

Key words: galaxies: active – quasars: emission lines – quasars: individual (3C390.3)

Online-only material: color figures

1. INTRODUCTION

The mass of supermassive black holes (SMBHs) is of fundamental importance for understanding active galactic nuclei (AGNs) which are powered by mass accretion onto an SMBH. Analysis of AGN variability by applying the technique of reverberation mapping (RM) has been established as a powerful tool to determine the size of the broad emission-line region (BLR) of AGNs (Blandford & McKee 1982; Horne et al. 2004; Netzer & Peterson 1997; Peterson 2003) and, under the assumption of virial gas motion, consequently the SMBH mass (e.g., Peterson et al. 2004).

Large observational efforts are required to obtain data of sufficient quality and temporal coverage to study AGN variability and to employ RM methods. Currently, about 50 AGNs have been monitored for periods of at least a few months, usually as part of international collaborations. The entire available database of reverberation observations obtained through 2003 was uniformly re-analyzed with improved methods of time series analysis to minimize systematic errors (Peterson et al.

2004). Some of these results have been superseded by more recent experiments (Bentz et al. 2006a, 2007; Denney et al. 2006, 2009b; Grier et al. 2008; Woo et al. 2010) and additional reverberation results steadily increase the size and quality of the database (e.g., Bentz et al. 2009b, 2010b; Denney et al. 2009a, 2010).

It has been shown that AGNs and non-active galaxies follow the same relation between the black hole mass, M_{bh}, and stellar velocity dispersion, σ_*, of the central spheroidal component of the host galaxy (Ferrarese et al. 2001; Gebhardt et al. 2000; Gültekin et al. 2009; Merritt & Ferrarese 2001; Tremaine et al. 2002) and that the masses based on RM studies are consistent with the masses derived from the M_{bh}–σ_* relation (Nelson et al. 2004; Onken et al. 2004; Woo et al. 2010). The close relations of the black hole mass with physical properties of the host galaxy, e.g., stellar velocity dispersion, bulge mass, and bulge luminosity, indicate a coupled growth of the black hole and the formation and evolution of the host galaxy (e.g., Silk & Rees 1998; Haiman & Loeb 1998, 2001; Bromm & Loeb 2003; Di Matteo et al. 2004; Yoo & Miralda-Escudé 2004; Volonteri & Rees 2006; Volonteri & Begelman 2010).

---

[*] Based on observations collected at the MDM Observatory.

The broad-line radio galaxy (BLRG) 3C 390.3 is a bright and nearby ($m_v = 15.0$, $z = 0.056$; Osterbrock et al. 1976) FR II radio galaxy with extended double-lobed radio emission (Leahy & Perley 1995). After the identification as optical counterpart of the radio source 3C 390.3 (Wyndham 1966), it was classified as an N-type galaxy by Sandage (1966). Soon, it was discovered that 3C 390.3 shows very broad Balmer emission lines (Lynds 1968) which were later recognized as prominent double-peaked emission-line profiles (Burbidge & Burbidge 1971). These double-peaked profiles are generally regarded as a characteristic signature of accretion disk emission (e.g., Eracleous & Halpern 1994, 2003; Gezari et al. 2007).

So far almost all AGN variability studies have focused on radio-quiet AGNs. However, 3C 390.3 has a well-known variability history (e.g., Cannon et al. 1968; Selmes et al. 1975; Barr et al. 1980; Penston & Perez 1984; Veilleux & Zheng 1991; Zheng 1996; Wamsteker et al. 1997; O'Brien et al. 1998; Dietrich et al. 1998; Sergeev et al. 2002; Tao et al. 2008) with photometric measurements going back to 1968 (Yee & Oke 1981). Using the Harvard plate collection, Shen et al. (1972) traced back brightness variations to 1895. Thus, 3C 390.3 was a prime target of a multiwavelength monitoring campaign in 1994/1995 especially because of previous reports of dramatic changes in the Balmer line profile shape and strength and to perform coordinated X-ray/UV/optical monitoring of a radio-loud AGN for the first time. Currently, 3C 120 and 3C 390.3 are the only radio-loud AGNs which have been monitored in detail. The multiwavelength study of 3C 390.3 in 1994/1995 (Leighly et al. 1997; O'Brien et al. 1998; Dietrich et al. 1998) shows significant variations in the X-ray, UV, and optical domain over a period of one year. However, the light curves of the UV and optical variations show a nearly monotonic increase of the continuum and emission-line flux with only moderately strong substructures. The measured delays of several broad emission lines relative to the observed continuum variations are about $\tau \simeq 20 \pm 6$ days for Hβ and Hα (Dietrich et al. 1998) and $\tau \simeq 36$ to 60 days (± 18 days) for C IV and Lyα (O'Brien et al. 1998). More recently, Sergeev et al. (2002) studied the variability characteristics of 3C 390.3 for a period of nearly one decade. They found a longer delay of the response of the Hβ emission with respect to continuum variations compared to the result of the 1994/1995 study. They concluded that the difference might be caused by different continuum variability characteristics which manifest in different continuum auto-correlation functions. Recently, Shapovalova et al. (2010), Jovanovic et al. (2010), Popovic et al. (2011), and Sergeev et al. (2011) discussed profile variations over periods from a few years up to about 15 years.

In the following work, we present the results of a monitoring campaign undertaken at MDM Observatory in late 2005. Based on imaging and spectroscopic data, we find that 3C 390.3 clearly showed broadband variations, delayed variations of the broad Balmer emission lines Hα, Hβ, and Hγ, and of the helium line He IIλ4686. Using the time delays and the peak separation in the rms spectra of these emission lines, we estimate a virial black hole mass of $M_{\rm bh}^{\rm vir} = 1.77^{+0.29}_{-0.31} \times 10^8 \, M_\odot$ for 3C 390.3 and using $\sigma_{\rm line}$ of the rms spectra $M_{\rm bh}^{\rm vir} = 2.60^{+0.23}_{-0.31} \times 10^8 \, M_\odot$, respectively. The detection of superluminal motion for 3C 390.3 indicates an inclination angle of $i = 27° \pm 2°$ which allows us to correct the observed velocity for the tilt of the line-emitting region relative to the observer. Taking this into account, we derive a black hole mass of $M_{\rm bh} = 0.86^{+0.19}_{-0.18} \times 10^9 \, M_\odot$ (peak separation) and $M_{\rm bh} = 1.26^{+0.21}_{-0.16} \times 10^9 \, M_\odot$ ($\sigma_{\rm line}$) for 3C 390.3, respectively,

Table 1
Imaging and Spectroscopy Observing Log of 3C 390.3

Civil Date[a]	Julian Date − 245 0000	
(mm dd yy)	Photom.	Spectros.
(1)	(2)	(3)
09 16 05	3630.71895	3630.74012
09 17 05	3631.68545	3631.71968
09 18 05	3632.67934	3632.69208
09 22 05	. . .	3636.67738
09 24 05	3638.60241	3638.61469
09 25 05	3639.60314	3639.61829
09 30 05	3644.61169	3644.63453
10 02 05	3646.58313	3646.60055
10 10 05	3654.65719	3654.64235
10 11 05	3655.60982	3655.59675
10 12 05	3656.60524	3656.59131
10 17 05	. . .	3661.61921
10 19 05	3663.61128	3663.59896
10 20 05	3664.62103	3664.60890
10 21 05	3665.60079	3665.58876
10 23 05	3667.56875	3667.58457
11 01 05	3676.57946	3676.59541
11 03 05	3678.59495	3678.58313
11 11 05	3686.58735	3686.57751
11 12 05	3687.57943	3687.56689
11 13 05	3688.57791	3688.56608
11 21 05	3696.55431	3696.57008
11 22 05	. . .	3697.63839
11 24 05	3699.61123	3699.63440
11 25 05	3700.55593	3700.56501
11 27 05	3702.57947	3702.56630
12 06 05	3711.59450	3711.58072
12 08 05	3713.56451	3713.58304

Note. [a] Beginning of the night.

which is, within the uncertainties, consistent with recent results based on the Ca II$\lambda\lambda$8494, 8542, 8662 stellar absorption triplet and the $M_{\rm bh}$–σ_* relation (Lewis & Eracleous 2006; Nelson et al. 2004).

2. OBSERVATIONS

We revisited 3C 390.3 to determine the size of the BLR with improved accuracy. In 2005 September until December we used the 2.4 m Hiltner telescope at MDM Observatory to obtain spectroscopic and imaging data (Table 1).

The instrumental setup of the Boller & Chivens CCD Spectrograph (CCDS) and imaging camera RetroCam (Morgan et al. 2005) was kept unchanged for the entire observing campaign to achieve a homogeneous data set, i.e., avoiding the impact of different instrumental settings. The spectrograph was equipped with a Loral 1200×800 pixel CCD, with a projected pixel size that corresponds to $0''.4 \, \rm pixel^{-1}$. To cover the entire optical wavelength range, a 150 grooves/mm grating was used with a fixed grating tilt for the entire observing season. The slit width was set to a uniform value of $3''$ and a position angle of P.A. = $90°$. To allow for correction of cosmic-ray event contamination, at each epoch two spectra were recorded for 3C 390.3 with an integration time of $t_{\rm int} = 900$ s each. In contrast to previous campaigns, we observed HD 217086 (BD+61°2373, O7Vn) for the entire campaign for flux calibration to minimize the uncertainty which is introduced by flux calibrations that are based on different standard stars. In addition, HD 217086 was employed to correct for strong atmospheric absorption bands, i.e., the

O_2 C band ($\sim$6275–6300 Å), O_2 B band ($\sim$6850–6950 Å), and broad H_2O absorption ($\sim$7160–7320 Å). This is especially important for the broad Hα emission-line profile which is severely affected by the B-band absorption. In total, optical spectra were recorded for 28 epochs (Table 1).

In addition, 3C 390.3 was simultaneously observed for 25 epochs in Sloan Digital Sky Survey (SDSS) g band (Fukugita et al. 1996) using RetroCam at the 2.4 m telescope (Table 1). RetroCam was equipped with a E2V CCD 55-20 (1152 × 770 pixel) with a pixel size of 22.5 μm, which corresponds to 0″.259 pixel^{-1}. The optical design of RetroCam provides the valuable option to switch between spectroscopic and imaging mode in less than 2 minutes. Thus, the g-band measurements were taken no more than a few minutes before the spectroscopic observations. The exposure time was uniformly set to $t_{int} =$ 120 s and generally one exposure was recorded.

The spectra of 3C 390.3 and the standard star HD 217086, as well as the g-band imaging data, were processed using MIDAS[8] software. Standard dark and flat-field corrections were applied to the spectra and g-band imaging data of 3C 390.3 and the HD 217086 spectra. We subtracted the night sky intensity for each spectrum individually. The night sky fit was based on two regions, $\sim$100″–130″ wide on average, which were separated by $\sim$60″ relative to the spectrum of 3C 390.3 and HD 217086, respectively. A third-order polynomial fit was used for each wavelength element to fit the spatial intensity distribution of the night sky emission.

Argon–xenon comparison spectra were recorded for each spectrum of 3C 390.3 for wavelength calibration, which is based on $\sim$15–20 individual lines. The wavelength calibration yields a sampling of (3.07 ± 0.05) Å pixel^{-1}. The spectral resolution, measuring the full width at half-maximum (FWHM) of isolated lines in the argon–xenon spectra, amounts to $R \simeq 280$ at $\lambda \simeq 5600$ Å. The spectra of 3C 390.3 were corrected for galactic reddening using $E_{B-V} = 0.072$ (Schlegel et al. 1998).

To transform the observed spectra into the rest frame of 3C 390.3, we measured a redshift of $z = 0.056 \pm 0.001$ which is based on the narrow emission lines of Hα, Hβ, [O I]λ6300, [O III]$\lambda\lambda$4959, 5007, and [O III]λ4363. In the following, we present the analysis of the rest-frame spectra of 3C 390.3 and discuss the results based on this spectra.

3. DATA ANALYSIS

3.1. g-band Imaging

We used the flat-field-corrected images to measure the g-band flux of 3C 390.3 relative to comparison stars in the field. The approach of relative photometry has the advantage of being quite insensitive to weather conditions, i.e., photometric conditions are not required. The BLRG 3C 390.3 is among a sample of 34 AGNs that were carefully studied by Penston et al. (1971). They provide Johnson U, B, V magnitudes for three non-variable stars in the field of 3C 390.3. RetroCam which has a field of view of 5′.0 × 3′.3 allows us to observe stars A and B together with 3C 390.3 (Figure 1). However, with an apparent brightness of $m_V = 11^{m}.71$, star A is usually saturated in the observed g-band frames. Star B has a magnitude ($m_V = 14^{m}.28$) comparable to that of 3C 390.3. This star was already successfully employed in a prior monitoring campaign of 3C 390.3 as a flux standard (Dietrich et al. 1998). Hence, we used star B to determine the relative broadband flux changes of 3C 390.3.

---

[8]　Munich Image Data Analysis System, trademark of the European Southern Observatory.
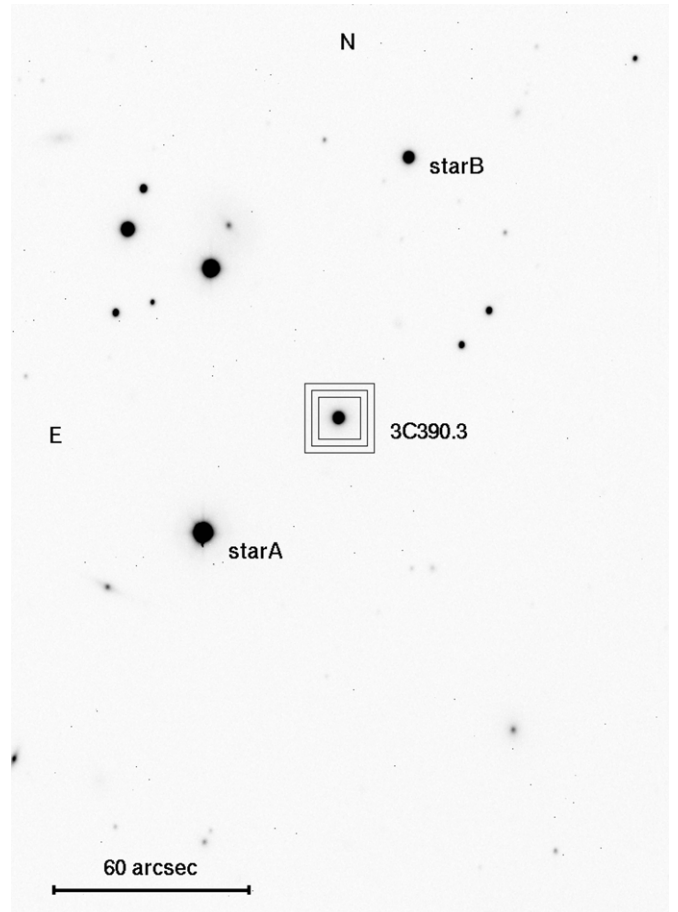
Figure 1. Typical g-band image of the field of 3C 390.3, taken with RetroCam on 2005 September 25 ($t_{int} = 120$ s). 3C 390.3 and the comparison stars are marked. In addition, the aperture and the location and size of the region which we used to correct for the sky background are shown.

To measure the g-band flux of 3C 390.3 and of star B, we applied a square aperture with a size of 13″ × 13″ (Figure 1). By using such a large aperture for the comparison star and particularly for 3C 390.3 we ensured that the total flux is recorded independently of the seeing, which varied from 1″.1 to 2″.7 with an average of (1″.7 ± 0″.4) during this monitoring campaign. To correct for the night sky flux, the object aperture was separated by a 2″ wide region (so-called no-man's-land) from a 2″ wide region that enclosed the square aperture (Figure 1). This outer region provided an average sky brightness which was used to correct the observed flux of the object for the night sky contribution.

3.2. Optical Spectroscopy

3.2.1. Intercalibration of the 3C 390.3 Spectra

To study broad emission-line flux variations, it is necessary to calibrate the spectra to a uniform flux level. This can be achieved using the flux of forbidden narrow emission lines from the narrow-line region (NLR). Due to the large spatial extension of the NLR (of the order of 100 pc in Seyfert galaxies) and the long recombination timescales which are due to the low gas density of the NLR ($\tau_{rec} \approx 100$ years for $n_e \approx 10^3$ cm^{-3}), light travel-time effects and long recombination timescales will damp out short timescale variability. Thus, it can be assumed that the flux of narrow emission lines can be treated as constant, at least on timescales of years to decades (e.g., Peterson 1993, 2000).

However, 3C 390.3 needs careful additional attention. The NLR of 3C 390.3 seems to be very compact (Baum et al. 1988; Sergeev et al. 2002) and the small emission-line flux ratio of F([O III]$\lambda\lambda$4959, 5007) to F([O III]λ4363) indicates the presence of high density gas ($n_e \simeq 10^5$ cm^{-3}). Furthermore, narrow-line variability has been reported for this object. Clavel & Wamsteker (1987) analyzed the strength of the narrow Lyα and C IVλ1549 emission lines. They found that the strength of these two narrow lines decreased by a factor of about 2–3 from 1978 to 1986. On the basis of optical spectra obtained between 1974 and 1990, Zheng et al. (1995) presented evidence that the fluxes of [O III]$\lambda\lambda$4959, 5007 follow continuum variations, although on a longer timescale than the broad emission lines. During the period of decreasing or increasing [O III] flux, there might also be periods of several months or years of nearly constant [O III] flux. Hence, we examined the data closely to test for variability of the [O III] emission lines before we used them for flux calibration.

To test the reliability of the narrow [O III] emission lines as an internal calibrator, the g-band imaging data are of great value. As noted earlier, these broadband flux measurements were taken nearly simultaneously with the spectra, i.e., within minutes of the spectral observations (Table 1) and the g-band brightness of 3C 390.3 was measured with high precision (see Section 4.2; ∼0.1%). To compare the g-band variations to those which can be derived from the spectral data, the spectra were convolved with the transmission curve of the SDSS g-band filter. The fluxes of the convolved spectra were measured for the transmission wavelength range of the g-band filter curve ($\lambda = 4000$–6000 Å). To adjust the flux level of the spectra to the g-band measurements, the spectra were rescaled. These scaling factors are on average (1.10 ± 0.07).

We used these adjusted spectra, based on the observed g-band flux variations, to test whether the [O III]λ5007 emission-line flux was constant during this monitoring campaign. Although the broadband flux measurements include the broad and narrow Hβ emission-line flux, as well as the [O III]$\lambda\lambda$4959, 5007 line emission, the contribution of emission-line variability to photometric variations can be neglected (Walsh et al. 2009) if it amounts to less than ∼10% of the broadband flux. For 3C 390.3, we find that the Hβ flux amounts to less than 5% of the g-band flux. To test the assumption that the [O III]λ5007 emission-line flux was constant for the duration of this monitoring campaign, these adjusted spectra were internally flux calibrated by scaling each individual spectrum to a uniform flux of the [O III]λ5007 emission line. First, we calculated a mean spectrum which was used as a reference spectrum. Next, we applied a modified version of the scaling algorithm of van Groningen & Wanders (1992) to adjust the flux of the [O III]λ5007 in the individual spectra to the reference spectrum. This routine minimizes the residuals of the [O III]λ5007 in a difference spectrum which is calculated for each spectrum with the reference spectrum. The intercalibration to a uniform flux level was achieved by allowing different flux scales, small wavelength shifts, and different spectral resolutions. The average scaling factor amounts to (0.99 ± 0.02). This result indicates that the [O III]λ5007 flux was constant in the adjusted spectra with a flux of F([O III]λ5007) = (189 ± 4) × 10^{-15} erg s^{-1} cm^{-2} (Table 2). It is interesting to note that during the monitoring campaign of 3C 390.3 in 1995 (Dietrich et al. 1998), the [O III]λ5007 emission-line flux was measured to be F([O III]λ5007) = (161 ± 4) × 10^{-15} erg s^{-1} cm^{-2} (rest frame flux) which is about ∼15% lower. This indicates that the [O III]λ5007 emission-line flux was lower

Table 2
Mean NLR Emission-line Rest-frame Fluxes, Relative to the Flux of Hβ

Line (1)	Flux$_{obs}$[a] (2)	Flux$_{cor}$[a,b] (3)
[O II]λ3727	1.18 ± 0.08	1.41 ± 0.10
[Ne III]λ3869	1.20 ± 0.08	1.41 ± 0.10
[Ne III]λ3968	0.73 ± 0.02	0.84 ± 0.02
Hγ λ4340	0.44 ± 0.02	0.48 ± 0.02
[O III]λ4363	0.85 ± 0.02	0.92 ± 0.03
He IIλ4686	0.15 ± 0.01	0.15 ± 0.01
Hβ λ4861	1.00 ± 0.01	1.00 ± 0.02
[O III]λ4959	2.48 ± 0.02	2.44 ± 0.05
[O III]λ5007	7.30 ± 0.07	7.12 ± 0.15
[Fe VII]λ5721	0.15 ± 0.01	0.13 ± 0.01
He Iλ5876	0.15 ± 0.01	0.13 ± 0.01
[Fe VII]λ6087	0.36 ± 0.02	0.30 ± 0.02
[O I]λ6300	0.99 ± 0.01	0.82 ± 0.02
[O I]λ6364	0.33 ± 0.01	0.27 ± 0.01
[Fe X]λ6374	0.06 ± 0.01	0.05 ± 0.01
[N II]λ6548	0.44 ± 0.01	0.35 ± 0.01
Hα λ6563	3.53 ± 0.07	2.85 ± 0.08
[N II]λ6583	1.34 ± 0.04	1.08 ± 0.04
[S II]λ6716	0.20 ± 0.01	0.16 ± 0.01
[S II]λ6731	0.22 ± 0.01	0.18 ± 0.01

Notes.
[a] Integrated Hβ-narrow line flux, F(Hβ) = (26.50 ± 0.19) × 10^{-15} erg s^{-1} cm^{-2}.
[b] Line ratios are reddening corrected assuming a Balmer decrement of F(Hα)/F(Hβ) = 2.85.

in 1995 compared to 2005 when 3C 390.3 was in a less luminous state. Based on the average scaling factor and the small scatter, it is justified to assume that the F([O III]$\lambda\lambda$4959, 5007) emission-line flux was constant during this monitoring campaign.

While the Hβ–[O III]$\lambda\lambda$4959, 5007 region is scaled with respect to the narrow [O III]λ5007 line, we investigated whether this internal calibration holds for the Hα region at longer wavelengths and the Hγ–[O III]λ4363 region at shorter wavelengths. We intercalibrated the spectra for the Hα region with respect to the fluxes of the relatively strong [O I]λ6300 emission line and the Hγ–[O III]λ4363 region using the narrow [O III]λ4363 emission line. We found that the Hα region required small adjustments to achieve a constant [O I]λ6300 flux. The average scaling factor for the Hα region amounts to (1.014 ± 0.021). For the Hγ–[O III]λ4363 region, minor rescaling of the spectra was also necessary. These scaling factors are on average (1.014 ± 0.004).

3.2.2. Accounting for Host Galaxy and Optical Fe II Emission

A spectrum of an AGN is the superposition of various sources, including the host galaxy, thermal and non-thermal continuum emission from the AGN, which can be described by a power-law continuum, Balmer continuum emission, Fe II line emission, and emission from other metal line transitions, e.g., carbon, nitrogen, oxygen, magnesium, neon, sulfur. These contributions need to be accounted for in order to obtain reliable line measurements and the strength of the AGN continuum that most of our study relies on. We adopted a multi-component fit approach (e.g., Wills et al. 1985) that we have successfully applied in prior studies of high-z quasars and narrow line Seyfert 1 (NLS1) galaxies (for more details, see Dietrich et al. 2002, 2003, 2005, 2009). We assume that the spectrum of 3C 390.3 can be

described as a superposition of three components: (1) a power-law continuum ($F_\nu \sim \nu^\alpha$), (2) a host galaxy spectrum (Kinney et al. 1996), and (3) a pseudo-continuum due to merging Fe II emission blends.

Neither a Balmer nor a Paschen continuum emission were taken into account because the Balmer edge at $\lambda = 3645$ Å is close to the short wavelength end of our spectra of 3C 390.3 and the strength of the Paschen continuum is only weakly constrained (Korista & Goad 2001).

As demonstrated by Bentz et al. (2006b, 2009a), it is crucial to correct for the host galaxy contribution to measure the strength of the AGN continuum flux density. Based on Advanced Camera for Surveys/*Hubble Space Telescope* (ACS/*HST*) images which were obtained for 14 AGNs of the AGN-watch sample (Peterson et al. 2004), Bentz et al. (2009a) estimated the host galaxy contribution to the continuum flux density at $\lambda = 5100$ Å for those AGNs, including 3C 390.3. For the large aperture of ($3'' \times 9\rlap{.}''4$) which we used, the galaxy contribution amounts to $F_{\rm gal}(5100\,\text{Å}) = (0.87 \pm 0.09) \times 10^{-15}$ erg s^{-1} cm^{-2} Å^{-1}, based on ACS/*HST* imaging data (M. C. Bentz 2008, private communication). The average host galaxy contribution which we determined, based on the multi-component fits, is $F_{\rm gal}^{\rm obs}(5100\,\text{Å}) = (0.77 \pm 0.10) \times 10^{-15}$ erg s^{-1} cm^{-2} Å^{-1}, i.e., within the errors consistent with the measurements based on the ACS image. To construct representative host galaxy template spectra, we combined several individual spectra of various Hubble types. These galaxy spectra were retrieved from the publicly available sample published by Kinney et al. (1996). The spectral resolution of these galaxy spectra amounts to $R \simeq 8$ Å which is comparable to the spectral resolution of our spectra.

To account for Fe II emission, we used the rest-frame optical Fe II template that is based on observations of I Zw1 by Boroson & Green (1992) which cover the wavelength range from 4250 Å to 7000 Å. An alternative optical Fe II emission-line template was presented by Véron-Cetty et al. (2004) which in addition takes into account NLR contributions to the Fe II emission. In general, these two templates are similar but in detail they differ at around $\lambda \simeq 5000$ Å and $\lambda \gtrsim 6400$ Å. The optical Fe II emission in the spectrum of 3C 390.3 is weak, however, and the width of the Fe II emission is expected to be quite broad, as is seen for other permitted emission lines. Therefore, the choice of the Fe II emission template has no impact on the results of this study.

Components (1), (2), and (3) were simultaneously fitted to the spectra of 3C 390.3 that were intercalibrated with respect to the [O III]$\lambda\lambda$4959, 5007 emission-line flux, to determine the minimum χ^2 of the fit. Various host galaxy templates were employed and the best results were obtained using an appropriately scaled spectrum of the E0 galaxy NGC 1407, which is consistent with the morphological type of the host galaxy of 3C 390.3. The width of the Fe II emission template was allowed to vary from FWHM = 3000 km s^{-1} up to 9000 km s^{-1} in steps of ΔFWHM = 500 km s^{-1}. The best-fit results were achieved for Fe II emission templates whose width was on average FWHM = (6000 ± 1000) km s^{-1}, ranging from FWHM = 5000 km s^{-1} to FWHM = 8500 km s^{-1}. In Figure 2, we show the fit for a typical spectrum of 3C 390.3 from this study to illustrate the method to determine the different components.

The uncertainty of the fit was estimated based on the distribution of χ^2 around the minimum. The spectral slope α of the continuum fit has an average error of $\Delta\alpha \simeq 0.01$, while the uncertainties in the continuum flux density at $\lambda = 5100$ and the Fe II emission flux are of the order of ~5%. The best fit of
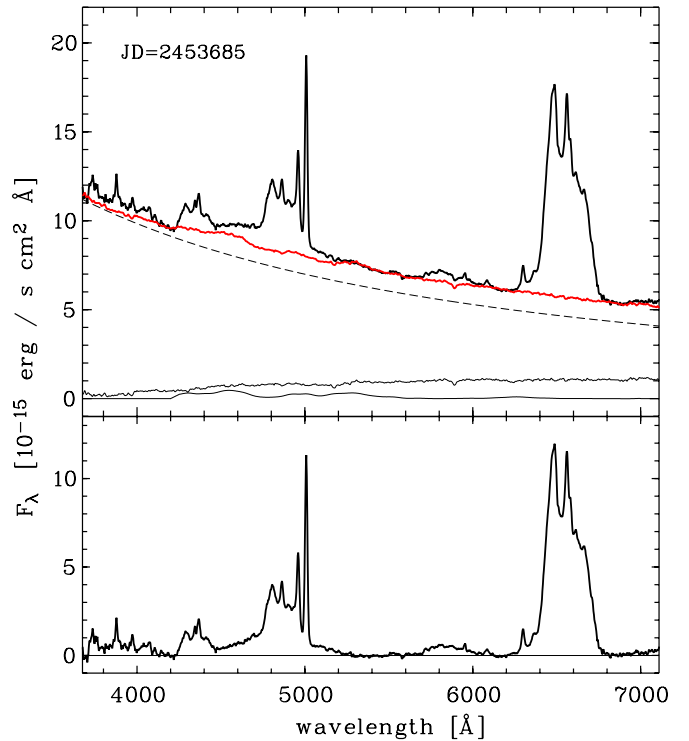
Figure 2. Decomposition of a spectrum of 3C 390.3, observed on 2005 November 11. In the top panel, the rest-frame spectrum is shown together with the power-law continuum fit (dashed line), the host galaxy fit (upper thin solid line), the optical Fe II emission fit (lower thin solid line), and the resulting combined fit (red line). In the bottom panel, the residual spectrum is displayed which shows the pure emission-line spectrum of 3C 390.3.

(A color version of this figure is available in the online journal.)

components (1) to (3) were subtracted before we continued to analyze the emission-line profiles of interest.

3.3. Narrow-line Region Emission Lines

The spectrum of 3C 390.3 shows strong narrow-line emission (Figure 2). Hence, it is necessary to correct the broad emission lines for NLR contributions before line flux and profile parameters are measured. In addition, the study of the narrow emission lines provide information about the ionizing continuum strength. Under the assumption that the NLR emission is constant during the observing period in 2005 (September to December), we measured the line strength of the narrow emission lines in the individual spectra of the entire campaign. This is an additional test for the quality of the intercalibration of the spectral region of the broad emission lines, studied for variability.

We used a strong NLR emission line as a template profile to fit the narrow-line spectrum and determine its flux (e.g., Whittle 1985c; Dietrich et al. 2005). Using high-quality, high-resolution spectra, Whittle (1985a, 1985b) showed that NLR emission-line profiles are similar and in particular that the Balmer emission-line profiles are identical to the [O III]λ5007 line profile within the uncertainties, even in the case of strong profile asymmetries. Therefore, we used the strong emission-line profile of [O III]λ5007 to obtain a representative NLR line profile template. To obtain such a profile template, we made use of a spectrum of 3C 390.3 which we observed with the 2.2 m telescope at Calar Alto Observatory/Spain (1994 August 30). At this time 3C 390.3 was at a lower intensity level than in 2005, i.e., the narrow emission lines are more pronounced (Figure 3).
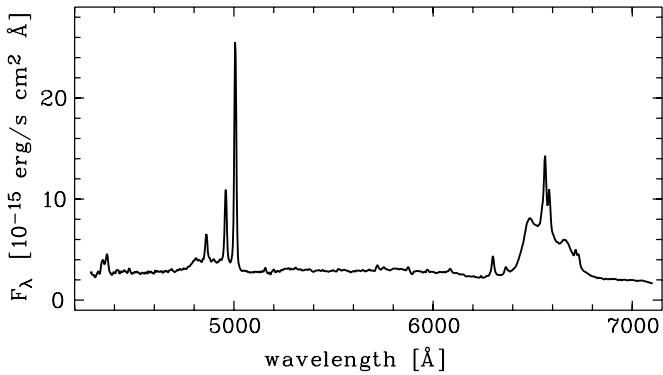
Figure 3. Spectrum of 3C 390.3 during a low state (1994 August 30, 2.2 m at Calar Alto Observatory/Spain).
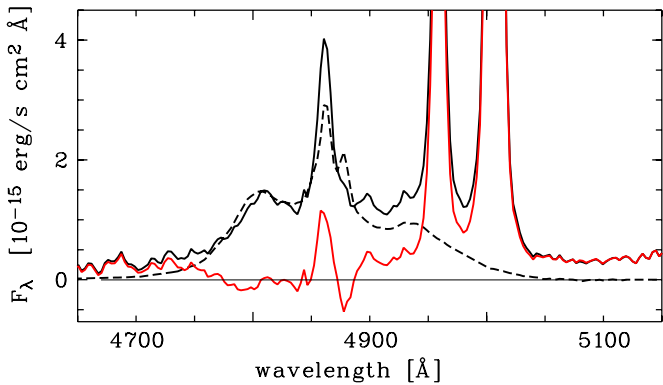
Figure 4. Hβ–[O III]λλ4959, 5007 emission-line complex of the spectrum shown in Figure 3 (thick line). The scaled Hα profile is shown as a long dashed line. The residual spectrum, which is used to fit the [O III] emission-line profiles, is shown as the red line.

(A color version of this figure is available in the online journal.)

This spectrum, which covers a wavelength range comparable to this study, has the advantage of a higher spectral resolution ($R \simeq 700$ at $\lambda \simeq 6500$ Å).

To isolate the [O III] emission lines which are located in the extended red wing of the double-peaked Hβ line profile we used an appropriately scaled Hα profile to recover the red wing of Hβ. This scaled Hα profile was subtracted and the residual was used to fit the [O III]λλ4959, 5007 line profiles (Figure 4). The [O III] line profiles are well described using a dominant narrow Gaussian component (FWHM = 11.0 Å ± 0.1 Å) and a broader Gaussian component (FWHM = 26.0 Å ± 1.5 Å) which is slightly blueshifted by $v_{\text{shift}} \simeq 100$ km s^{-1}, to account for the base of the line profile (Figure 5). We find that the narrow component carries ∼75% of the [O III]λ5007 emission-line flux. The individual Gaussian components have a priori no physical meaning by themselves, but are just used to obtain an NLR line profile template.

4. RESULTS

4.1. The Narrow-line Region Spectrum

The [O III]λ5007 emission-line profile fit (Section 3.3) was used to measure the NLR emission-line flux of the narrow lines in the spectra of 3C 390.3. While the NLR emission-line profile was kept fixed, we allowed the strength of the profile template to vary and also allowed variations of the profile width and the location in wavelength space. For measurable emission-line doublets, we assumed that the line ratios are $F([\text{O III}]\lambda 5007)/$
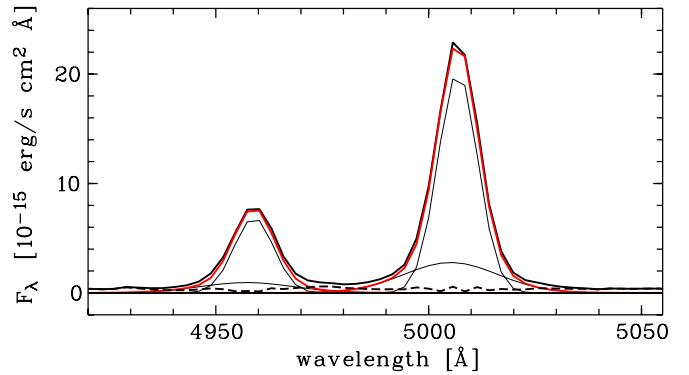
Figure 5. Fit of the [O III]λ4959 and [O III]λ5007 emission-line profiles employing a strong narrow and a weaker, slightly blueshifted broader Gaussian component for each line (thin black lines). The resulting fit is shown as a thick red line which recovers the observed spectrum well, as can be seen by the residuum (dashed line).

(A color version of this figure is available in the online journal.)

$F([\text{O III}]\lambda 4959) = 2.94$, $F([\text{O I}]\lambda 6300)/F([\text{O III}]\lambda 6364) = 3.05$, and $F([\text{N II}]\lambda 6583)/F([\text{N II}]\lambda 6548) = 3.06$ (Osterbrock & Ferland 2005) in order to fit the weaker line of each doublet.

Applying this approach we measured the strength of the emission lines and listed them in Table 2. The measurement uncertainty for an individual spectrum is of the order of ∼5% for strong narrow emission lines like [O III]λλ4959, 5007. In the case of moderately strong lines like the [O I]λ6300, [O II]λ3727, [Ne III]λ3869, and blended lines like [N II]λλ6548, 6583 the error is of the order of ∼10% or less, while for the weakest lines it is ∼25%, e.g., [Fe x]λ6374, [S II]λλ6716, 6731. In Table 2, we present the mean narrow emission-line fluxes as measured for all epochs and the scatter of the distribution.

We corrected the observed line fluxes for internal reddening before the emission-line flux ratios were analyzed. Generally, it is assumed that the observed Balmer decrement, i.e. $F(\text{H}\alpha)/F(\text{H}\beta)_{\text{obs}}$, can be used to estimate the internal reddening (e.g., Davidson & Netzer 1979; Netzer 1982). However, there are strong indications that the intrinsic Balmer decrement of the emission-line gas of AGNs is about $F(\text{H}\alpha)/F(\text{H}\beta) = 3.1$ instead of the classical case B value for the BLR due to collisional enhancement in the higher density partially ionized zone (e.g., Gaskell & Ferland 1984; Halpern & Steiner 1983; Netzer 1982).

For the NLR gas the strength of the [O II]λ3727 emission indicates the presence of a large fraction of low density gas ($n_e^{\text{crit}}(O^+) = 3.1 \times 10^3$ cm^{-3} for $2D_{5/2}$ and $n_e^{\text{crit}}(O^+) = 1.6 \times 10^4$ cm^{-3} for $2D_{3/2}$; Osterbrock & Ferland 2005). Thus, additional collisional enhancement, particularly of Hα emission, is expected to be weak. Therefore, we used the classical value of the Balmer decrement of $F(\text{H}\alpha)/F(\text{H}\beta)_{\text{int}} = 2.85$, for the pure recombination case B (e.g., Osterbrock & Ferland 2005) to correct the narrow emission-lines for reddening (e.g., Crenshaw et al. 2001). We determine an $E_{B-V} = 0.205 \pm 0.004$ for the NLR of 3C 390.3. Together with a Galactic reddening curve (Seaton 1979), we corrected the observed emission-line ratios relative to $F(\text{H}\beta)$, applying

$$\frac{F(\text{line})}{F(\text{H}\beta)}_{\text{int}} = \frac{F(\text{line})}{F(\text{H}\beta)}_{\text{obs}} \times 10^{0.4\,E_{B-V}\,(R_\lambda - 3.68)} \quad (1)$$

with R_λ as the Galactic extinction coefficient at the wavelength of the corresponding emission line (Seaton 1979). We also investigated the impact of a larger Balmer decrement, $F(\text{H}\alpha)/F(\text{H}\beta) = 3.1$, which has been suggested to be more

typical for emission-line ratios of the BLR, i.e., it takes into account collisional excitation and radiative transfer effects (Osterbrock & Ferland 2005). We find that it results in reddening-corrected line ratios that are less than ∼8% larger for line ratios shortward of Hβ and less than ∼8% smaller for line ratios longward of Hβ. The reddening-corrected narrow emission-line measurements (flux$_{cor}$) are given in Table 2.

4.2. Continuum Variability

We measured the relative broadband flux variations of 3C 390.3 relative to the calibrated comparison star B in the field of 3C 390.3 (Figure 1). The Johnson V magnitude of this star is given as $m_V = 14.28$ (Penston et al. 1971). During the monitoring campaign, star B and 3C 390.3 showed comparable g-band brightness. This already indicates that 3C 390.3 was in a brighter state during this monitoring campaign in late 2005 than in 1995 (Dietrich et al. 1998).

Based on the measured g-band flux ratios, we calculate the g-band magnitude variations of 3C 390.3. To do this, we utilized the known V-band magnitude of comparison star B. Fukugita et al. (1996) and Smith et al. (2002) give the transformation of a g' band into V-band magnitude, which involves in addition the $(B − V)$ color. Applying these relations we find a g'-band magnitude of $m_{g'} = 14.59$ (Fukugita et al. 1996) and $m_{g'} = 14.62$ (Smith et al. 2002) for star B, respectively. However, we used the g-band filter of RetroCam (Morgan et al. 2005) at the MDM 2.4 m telescope to measure the broadband flux of 3C 390.3. It has been pointed out that there are small differences between the g'-band magnitudes (used at the 0.5 m telescope of the SDSS) and the g-band filter (used at the 2.5 m telescope of the SDSS; Tucker et al. 2006; Davenport et al. 2007; Smith et al. 2007).

Thus, we had to transform the g'-band magnitude of the comparison star B into a g-band magnitude. We employed the transformation given by Tucker et al. (2006) with $g = g' + 0.060 × ((g' − r') − 0.53)$. To get an estimate of the color $g' − r'$ we used the color of the star L107-S97 in Bilir et al. (2008) which has a very similar $(B − V)$ color to comparison star B. This results in a correction of $\Delta(g − g') = −0.0014$, which can be neglected. Therefore, for comparison star B the g band and the g'-,band magnitudes can be treated as identical. In Figure 6 (top panel), we show the broad g-band flux density variations of 3C 390.3.
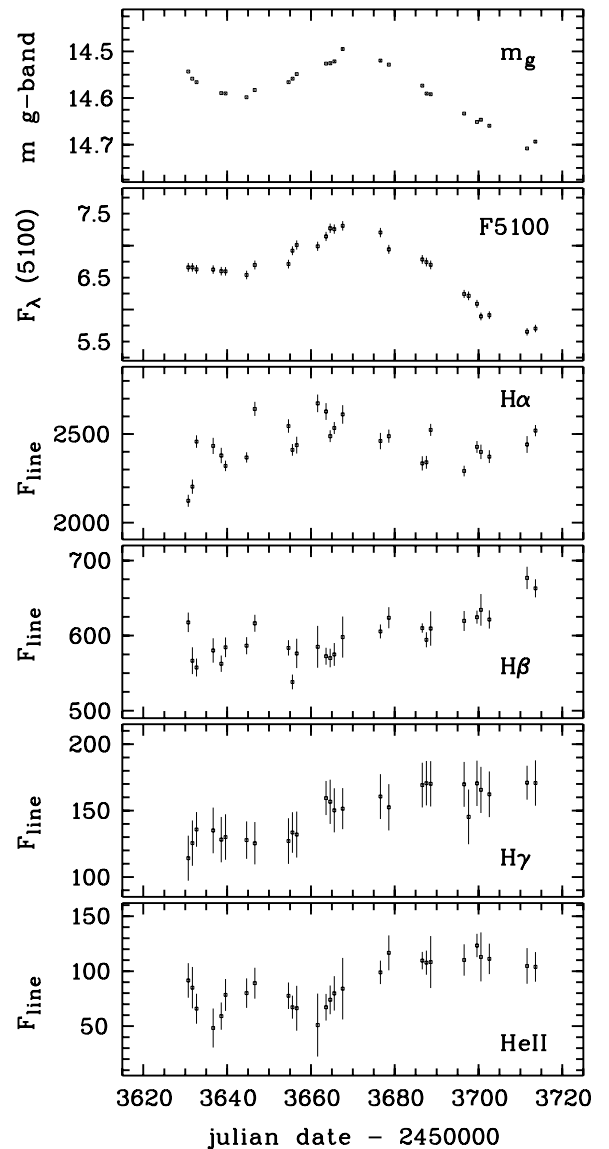
The errors of the g-band magnitudes of 3C 390.3 and comparison star B are estimates using the uncertainties of the flux measurements. These uncertainties are combined in quadrature to obtain the error of the flux ratio and hence of the flux density of 3C 390.3. Due to the high integrated count rates of comparison star B and of 3C 390.3, in the range of several 10^6 counts, the errors of the flux ratios are of the order of ∼0.1%.

Next, we measured the continuum flux density variations at $\lambda = 5100$ Å directly from the power law continuum fit for each spectrum (Table 3). In Figure 6, the variations of $F_\lambda(5100$ Å$)$ are displayed. It can be seen that the AGN continuum and the g-band variations follow the same pattern and have comparable amplitudes.

4.3. Broad Emission-line Flux Variations

4.3.1. Hα λ 6563

In the spectral region of the broad and double-peaked Hα emission line some of the corrected spectra still exhibit a weak residual continuum flux level. To adjust for the residual continua,

Figure 6. Light curves of 3C 390.3 for the g band (in g-band magnitudes), the $F_\lambda(5100$ Å$)$ AGN continuum (in units of 10^{-15} erg s^{-1} cm^{-2} Å^{-1}), and the variations of the broad emission-line fluxes of Hα, Hβ, Hγ, and He II λ4686 (displayed in units of 10^{-15} erg s^{-1} cm^{-2}). The uncertainties of the g-band magnitudes are smaller than the plot symbol.

we fit a linear local pseudo-continuum. The Hα emission-line flux was measured within the wavelength range of 6200–6800 Å. This spectral range contains contributions of several narrow emission lines, including Hα$_{nar}$. To correct for narrow-line flux contamination, the average intensities of the narrow emission lines of [O I]λλ6300, 6364, [Fe x]λ6374, [N II]λλ6548, 6583, [S II]λλ6716, 6731, and Hα$_{nar}$ were subtracted (Table 2) and the resulting broad Hα emission-line flux is given in Table 3.

To estimate the uncertainties of the broad Hα flux measurements, first the uncertainties of the multi-component fit were taken into account. As noted earlier, we assumed that the strength of the power law continuum fit, the host galaxy contribution, and the optical Fe II emission can be determined within 1%. The next source of error is given by the uncertainties of the narrow emission-line intensities (Table 2). The largest source of error is the level of the pseudo-continuum. The strength of the linear pseudo-continuum fit is based on two windows which are located at 6135–6160 Å and 6875–6895 Å, respectively.

Table 3
Observed *g*-band Magnitudes, Measured Rest-frame Continuum Flux Density at $\lambda = 5100$ Å, and
Integrated Flux of the Broad Emission Lines of Hα, Hβ, Hγ, and He IIλ4686

Julian Date − 245 0000 (1)	*g*-band (mag) (2)	Julian Date -245 0000 (3)	F_λ5100 Å[a] (4)	Hα λ6563[b] (5)	Hβ λ4861[b] (6)	Hγ λ4340[b] (7)	He IIλ4686[b] (8)
3630.71895	14.543 ± 0.001	3630.74012	6.66 ± 0.07	2123.4 ± 33.7	617.7 ± 13.0	114.2 ± 17.0	91.6 ± 15.7
3631.68545	14.559 ± 0.001	3631.71968	6.66 ± 0.07	2203.3 ± 40.3	566.6 ± 17.8	125.5 ± 17.1	85.0 ± 18.8
3632.67934	14.566 ± 0.001	3632.69208	6.63 ± 0.07	2457.7 ± 35.3	557.5 ± 12.0	135.8 ± 13.1	65.9 ± 13.7
. . .	. . .	3636.67738	6.63 ± 0.07	2433.4 ± 45.7	580.2 ± 16.4	135.0 ± 17.2	48.4 ± 17.7
3638.60241	14.589 ± 0.001	3638.61469	6.60 ± 0.07	2379.1 ± 43.4	562.5 ± 10.9	128.2 ± 17.1	59.1 ± 12.4
3639.60314	14.590 ± 0.001	3639.61829	6.60 ± 0.07	2320.6 ± 29.5	584.4 ± 13.1	130.1 ± 17.1	78.4 ± 14.5
3644.61169	14.598 ± 0.001	3644.63453	6.54 ± 0.07	2368.3 ± 29.3	586.6 ± 11.4	127.8 ± 14.0	80.0 ± 13.3
3646.58313	14.583 ± 0.001	3646.60055	6.70 ± 0.07	2642.3 ± 39.7	616.4 ± 11.3	125.4 ± 15.9	89.1 ± 14.0
3654.65719	14.566 ± 0.001	3654.64235	6.71 ± 0.07	2545.6 ± 38.1	583.7 ± 10.2	127.0 ± 17.2	77.6 ± 12.0
3655.60982	14.559 ± 0.001	3655.59675	6.92 ± 0.07	2410.9 ± 33.3	538.2 ± 9.8	133.5 ± 15.3	67.2 ± 10.5
3656.60524	14.549 ± 0.001	3656.59131	7.01 ± 0.07	2437.8 ± 47.5	576.2 ± 19.5	131.9 ± 17.3	66.3 ± 20.4
. . .	. . .	3661.61921	6.99 ± 0.07	2673.7 ± 49.6	585.2 ± 27.9	150.2 ± 35.8	51.0 ± 28.7
3663.61128	14.526 ± 0.001	3663.59896	7.14 ± 0.07	2627.9 ± 47.4	572.5 ± 11.3	159.4 ± 12.8	67.2 ± 12.1
3664.62103	14.525 ± 0.002	3664.60890	7.27 ± 0.07	2488.4 ± 33.6	570.2 ± 12.4	156.6 ± 16.6	73.9 ± 13.0
3665.60079	14.522 ± 0.002	3665.58876	7.26 ± 0.08	2534.5 ± 34.4	574.9 ± 15.2	150.2 ± 16.6	79.8 ± 15.7
3667.56875	14.495 ± 0.004	3667.58457	7.31 ± 0.08	2611.2 ± 52.2	598.1 ± 27.4	151.4 ± 15.5	84.0 ± 28.0
3676.57946	14.520 ± 0.002	3676.59541	7.20 ± 0.08	2460.7 ± 46.3	605.6 ± 9.2	160.6 ± 16.9	99.0 ± 10.7
3678.59495	14.529 ± 0.002	3678.58313	6.94 ± 0.07	2488.4 ± 37.3	623.8 ± 14.0	152.5 ± 17.5	116.7 ± 15.9
3686.58735	14.574 ± 0.001	3686.57751	6.78 ± 0.07	2334.8 ± 40.1	610.1 ± 6.2	169.2 ± 16.8	109.6 ± 7.9
3687.57943	14.591 ± 0.002	3687.56689	6.74 ± 0.07	2340.7 ± 36.4	594.4 ± 10.0	170.6 ± 16.7	107.7 ± 11.0
3688.57791	14.592 ± 0.002	3688.56608	6.70 ± 0.07	2523.8 ± 34.1	609.5 ± 22.9	170.2 ± 17.0	108.3 ± 23.7
3696.55431	14.633 ± 0.001	3696.57008	6.24 ± 0.07	2291.8 ± 30.0	619.6 ± 13.3	169.8 ± 16.9	110.2 ± 14.3
. . .	. . .	3697.63839	6.21 ± 0.07	2162.3 ± 40.4	632.8 ± 15.5	145.3 ± 20.6	110.2 ± 15.6
3699.61123	14.651 ± 0.002	3699.63440	6.09 ± 0.06	2427.7 ± 33.6	624.6 ± 8.6	170.5 ± 17.1	123.3 ± 10.6
3700.55593	14.647 ± 0.002	3700.56501	5.89 ± 0.06	2399.6 ± 40.6	634.3 ± 21.1	165.6 ± 17.4	113.0 ± 22.3
3702.57947	14.659 ± 0.002	3702.56630	5.91 ± 0.06	2372.6 ± 36.2	621.5 ± 12.2	162.2 ± 17.2	111.2 ± 13.8
3711.59450	14.708 ± 0.002	3711.58072	5.65 ± 0.06	2441.6 ± 47.4	676.9 ± 15.0	171.0 ± 12.8	104.8 ± 16.2
3713.56451	14.694 ± 0.002	3713.58304	5.70 ± 0.06	2519.7 ± 31.8	663.0 ± 12.0	170.7 ± 17.1	103.9 ± 13.5

Notes.
[a] Continuum flux in (10^{-15} erg s^{-1} cm^{-2} Å^{-1}).
[b] Integrated emission-line flux in (10^{-15} erg s^{-1} cm^{-2}).

Using the scatter of the continuum level of these two windows, the error introduced by the pseudo-continuum fit was determined. The individual errors were combined in quadrature to obtain the uncertainty of the individual broad Hα emission-line flux measurements (Table 3). In Figure 6, we present the light curve of the broad Hα emission-line flux. Although the scatter is larger than for the *g*-band and F_λ(5100 Å) variations, the broad Hα flux shows a similar variation pattern which is shifted to later epochs.

### 4.3.2. Hβ λ 4861 and He IIλ4686

As in the case of the Hα emission line, it was necessary to correct for a residual continuum level of the Hβ λ4861–He IIλ4686 wavelength range. The linear local pseudo-continuum fits are based on two 20 Å wide continuum regions centered at $\lambda = 4520$ Å and $\lambda = 5240$ Å, respectively. The corrected spectra were used to measure the broad Hβ λ4861 and He IIλ4686 emission-line fluxes. Because the emission-line profiles of 3C 390.3 are so broad (Figure 2) it is necessary to evaluate and to correct for the mutual blending of the Hβ λ4861 and He IIλ4686 emission, i.e., to identify the contributions of the Hβ λ4861 and He IIλ4686 emission in the overlapping region.

We used the broad Hα λ6563 emission-line profile as a template to estimate the shape and strength of the broad He IIλ4686 emission. To extract the broad Hα λ6563 emission-line profile, the mean spectrum of the campaign was used (Section 4.4) and the mean Hα profile was corrected for

the narrow emission-line contributions ([O I]$\lambda\lambda$6300, 6364, [Fe x]λ6374, [N II]$\lambda\lambda$6548, 6583, Hα_{nar}, and [S II]$\lambda\lambda$6716, 6731). The width of the double-peaked broad emission-line profile of Hα λ6563 was scaled to have the same width in velocity space at the location of the Hβ λ4861 emission line and the strength was rescaled to fit the central part and red wing of the Hβ λ4861 profile. In Figure 7 we show the Hβ λ4861–He IIλ4686 range corrected for narrow emission of He IIλ4686, Hβ λ4861, and [O III]$\lambda\lambda$4959, 5007. The scaled double-peaked Hα emission-line profile describes the broad Hβ λ4861 emission profile well, except the blue hump which is less prominent in the Hβ profile compared to the Hα λ6563 emission-line profile. This results in an absorption line-like feature in the residual spectrum (Figure 7, bottom panel) which indicates a steeper Balmer decrement for the blue peak in the double-peaked profiles. To measure the He IIλ4686 emission-line flux, the residual emission at the location of the He IIλ4686 line was fit with a rescaled broad Hα λ6563 double-peaked profile and also with a single broad Gaussian profile. The profile in the residual spectrum of the mean spectrum is better represented by a Gaussian profile than using an appropriately scaled double-peaked Hα profile (Figure 7). To determine an appropriate Gaussian profile for the broad He IIλ4686 emission, the blue wing of the He II line in the residuum was extracted and assuming that the broad He II profile is symmetric the blue wing was mirrored to represent the red wing of the He IIλ4686 line profile (Figure 8).
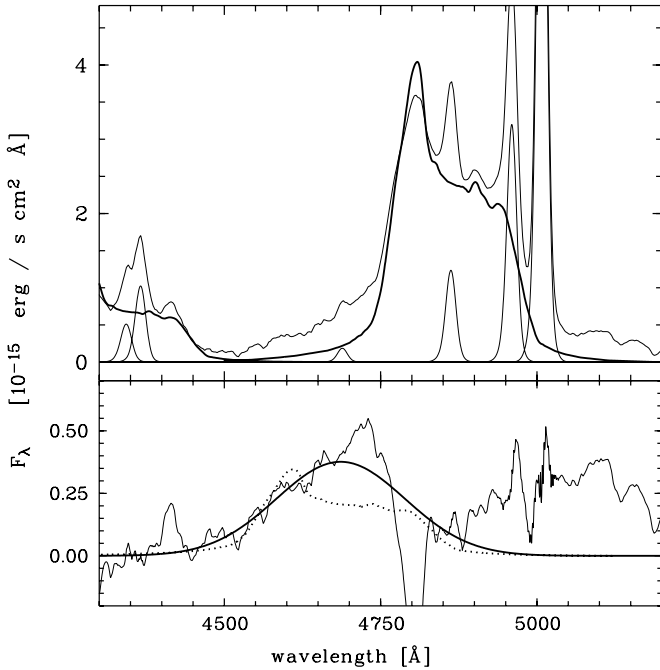
**Figure 7.** In the top panel, the Hβ–[O III]λλ4959, 5007 complex is shown together with the scaled broad, double-peaked profile fit of Hα for the Hβ and Hγ emission lines (thick line). In addition, the profile fits of the narrow emission lines for this wavelength range are displayed. In the bottom panel, the residual spectrum is presented after subtracting the profile fits of the narrow emission lines and the broad profile fits for Hβ and Hγ. The residual profile at the location of the He IIλ4686 emission line is reconstructed with a scaled double-peaked profile (dotted line) and with a Gaussian profile (thick line).

The resulting profile can be described with a single Gaussian profile at $\lambda_c = 4686.14$ Å ± 0.04 Å and a profile width of FWHM = 242.3 Å ± 1.4 Å (15,500 km s^{-1} ± 100 km s^{-1}). To measure the He IIλ4686 emission-line light curve (Figure 6) a Gaussian profile of fixed width (FWHM = 15,500 km s^{-1}) was fit to the blue wing of the He IIλ4686 profile in the spectra of 3C 390.3 (Figure 8). The flux of the He IIλ4686 emission was measured from this Gaussian fit for a wavelength range of $\lambda = 4472$ Å to $\lambda = 4900$ Å. This Gaussian profile fit was subtracted from the spectrum to measure the broad Hβ λ4861 emission flux in the range from $\lambda = 4680$ Å to $\lambda = 5000$ Å (Table 3). The resulting light curves for the broad Hβ λ4861 emission-line flux, corrected for narrow Hβ emission, and the He IIλ4686 emission line, are displayed in Figure 6.

To estimate the total error of these flux measurements, we assumed that the uncertainties of the multi-component fit are of the order of 1%. The errors introduced by the correction of the narrow emission lines are taken from Table 2. The uncertainty due to the broad He IIλ4686 emission is of the same order as the total error that is caused by the narrow emission lines. As in the case of Hα λ6563, the dominant source of error is the level of the pseudo-continuum fit. The level of the pseudo-continuum fit was varied within the scatter given by the two ranges centered at $\lambda_c = 4520$ Å and $\lambda_c = 5240$ Å that are 20 Å wide. The individual contributions to the uncertainty were combined in quadrature to obtain the total uncertainties of the individual broad Hβ and He IIλ4686 emission-line flux measurements (Table 3).

4.3.3. Hγ λ 4340

In the case of the Hγ emission-line profile region, we correct for a residual continuum level as well. The linear local
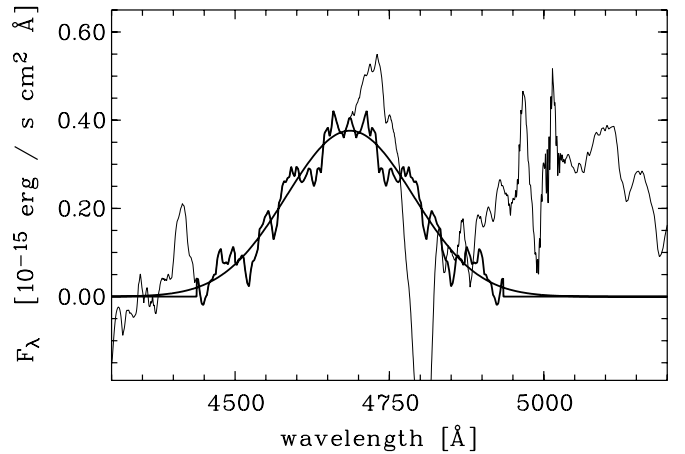
Figure 8. Gaussian profile fit for the He IIλ4686 emission-line profile, under the assumption that the blue wing can be used to represent the red wing (thick solid lines).

pseudo-continuum fits are based on two 20 Å wide continuum regions centered at $\lambda_c = 4160$ Å and $\lambda_c = 4530$ Å, respectively. The corrected spectra were used to measure the Hγ λ4340 emission-line flux (4220 Å to 4500 Å). These flux measurements were corrected for the emission-line contributions of the narrow Hγ λ4340 emission and of the [O III]λ4363 emission, using the average narrow line fluxes as given in Table 2. The resulting light curve of the variable broad Hγ λ4340 emission line is shown in Figure 6. The variability pattern is very similar to the broad Hβ variations.

To estimate the total error of the broad Hγ flux measurements (Table 3), we assumed that the uncertainties of the multi-component fit are of the order of 1%. The errors introduced by the correction of the narrow emission lines are taken from Table 2. The dominant source of error is the level of the pseudo-continuum fit. The level of the pseudo-continuum fit was varied within the scatter given by the two 20 Å wide ranges ($\lambda_c = 4160$ Å and $\lambda_c = 4530$ Å). The contributions of the individual error sources were combined in quadrature to estimate the total uncertainty of the broad Hγ λ4340 emission-line flux.

4.4. Mean and rms Spectra

4.4.1. Hα λ6563, Hβ λ4861, and Hγ λ4340

Based on the calibrated spectra of 3C 390.3, we calculated mean and residual (hereafter simply *rms*) spectra of the broad emission profiles of Balmer lines Hα, Hβ, and Hγ which are shown in Figure 9. These mean and rms spectra are based on the entire set of MDM spectra, except the spectrum that was recorded at the epoch JD = 244 3696. The signal-to-noise ratio (S/N) for this spectrum is significantly lower than for all the other spectra of 3C 390.3 on account of bad weather conditions (S/N$_{2443696} \simeq 10$, compared to an average S/N for the sample of S/N = 35 ± 7).

The mean spectra of the Balmer emission lines show a characteristic double-peaked emission-line profile with a strong blue hump while the red hump is very weak. The rms spectra of the Balmer lines show a similar shape. The blue hump is the dominant feature for the Hα and Hβ rms spectra while it is less pronounced for Hγ. Only weak residuals of narrow emission lines can be seen in the Balmer rms spectra of Hα, Hβ, and Hγ. The rms spectra of the Balmer emission lines also display extended red wings.
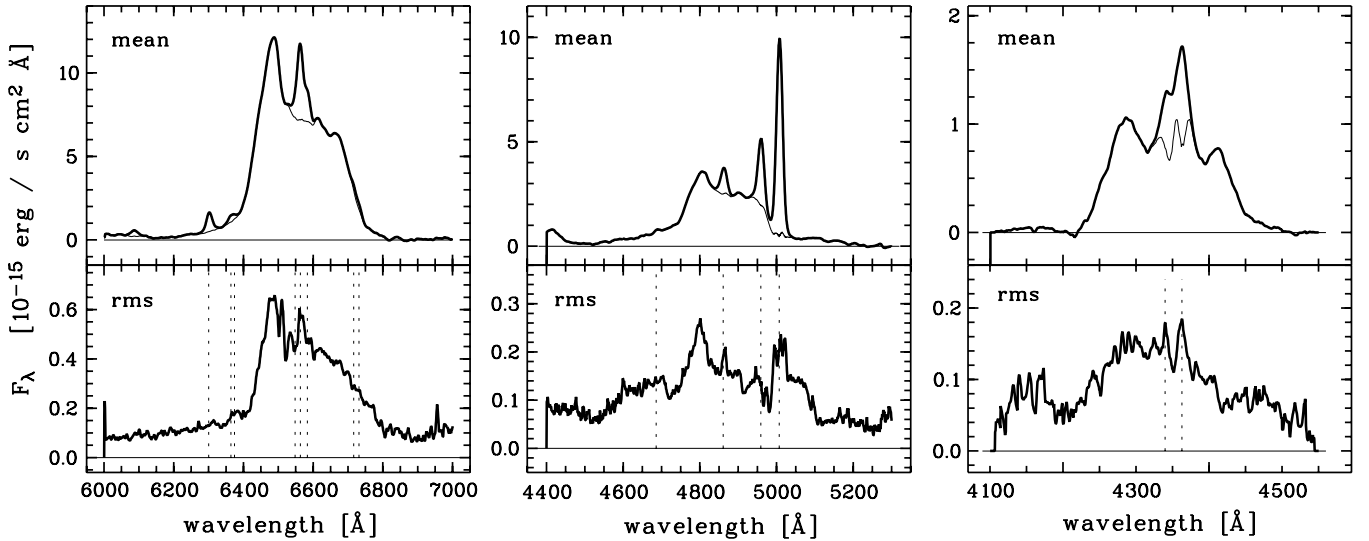
Figure 9. Mean and rms spectra of the hydrogen Balmer lines Hα, Hβ, and Hγ. The top panel shows the mean spectra (thick lines) and the narrow-line-subtracted mean spectra (thin lines). In the bottom panel, the rms spectrum is presented (solid line) together with the location of narrow emission lines (dotted lines).

Table 4
Measurements of the Mean and rms Line Profile Parameters of the
Balmer Lines Hα, Hβ, Hγ, and the Helium Line He II λ4686

Mean Spectra				
Feature	FWHM (Å)	σ_{line} (Å)	FWHM (km s^{-1})	σ_{line} (km s^{-1})
(1)	(2)	(3)	(4)	(5)
Hα λ 6563	275 ± 1	101 ± 1	12563 ± 31	4607 ± 29
Hβ λ 4861	214 ± 1	87 ± 1	13211 ± 28	5377 ± 37
Hγ λ 4340	172 ± 2	58 ± 1	11875 ± 103	3991 ± 29
He II λ4686	242 ± 8	103 ± 3	15480 ± 512	6590 ± 192
rms Spectra				
	FWHM (Å)	σ_{line} (Å)	FWHM (km s^{-1})	σ_{line} (km s^{-1})
Hα λ 6563	278 ± 33	106 ± 6	12679 ± 1312	4839 ± 215
Hβ λ 4861	176 ± 26	88 ± 5	10872 ± 1670	5455 ± 278
Hγ λ 4340	165 ± 19	75 ± 2	11422 ± 1458	5191 ± 82
He II λ4686	207 ± 15	80 ± 11	13244 ± 960	5125 ± 704

The line width can be characterized by its FWHM and by the line dispersion σ_{line} (the second moment of the line profile; e.g., Peterson et al. 2004). In order to characterize the uncertainties in each of these parameters we employed a procedure described by Peterson et al. (2004). For a set of N spectra, N spectra are randomly selected, in particular without regard whether the spectrum has been previously selected or not. These N randomly selected spectra are used to construct mean and rms spectra from which the line width measurements are made. This process yields one Monte Carlo realization, and a large number ($N \simeq 10,000$) of these realizations yield a mean and standard deviation for each of the measurements of the line width. The results of the line profile measurements and the corresponding errors are presented in Table 4.

We find that the mean spectra of the Balmer emission lines show a similar profile width of FWHM = 11,900–13,200 km s^{-1} and the second moment of the line profiles σ_{line} ranges from 4000 km s^{-1} to 5400 km s^{-1}, respectively. The comparison of the rms spectrum profile widths shows basically the same result. The Balmer emission-line rms spectra have an average profile

width of FWHM = (11430 ± 790) km s^{-1} and an average second moment of the line profiles of $\sigma_{line} = (5160 \pm 310)$ km s^{-1}, respectively.

4.4.2. He II λ4686

The mean and rms profiles are a Gaussian due to our approach to measure the He II λ4686 emission-line flux and hence also the rms spectrum (Section 4.3.2). However, the rms spectrum of the He II λ4686 variations is contained in the rms spectrum of the broad Hβ emission line (Figure 9). To recover the He II λ4686 rms spectrum we examined two approaches.

First, the fit of the He II λ4686 emission line was subtracted from each spectrum of the Hβ–[O III]λλ4959, 5007 emission-line region. This results in an uncontaminated broad Hβ profile. These spectra are used to calculate a mean and rms spectrum which represent the Hβ variation alone. In Figure 10 the mean spectrum of the Hβ–[O III]λλ4959, 5007 emission-line region with and without correction for the broad He II λ4686 emission is displayed, as well as the comparison of the rms spectra. The difference of these rms spectra can be associated with the He II λ4686 rms spectrum (Figure 10).

As an alternative approach to recover the He II λ4686 rms spectrum, we assumed that the rms spectrum of the broad Hα emission line can be used as a template for the rms spectrum of the Hβ emission line. The Hα rms spectrum was re-binned that the width is unchanged in velocity space at the location of the Hβ emission line. In Figure 11, the rms spectra of the broad Hβ and Hα emission lines are shown. Next, the re-binned Hα rms spectrum was rescaled by dividing by 3.50 to fit the red wing of the Hβ rms spectrum. The difference between the Hβ rms spectrum and the scaled, re-binned Hα rms spectrum can be associated with the He II λ4686 rms spectrum as well. This difference is displayed in the bottom panel of Figure 11. It can be seen that this representation of the He II λ4686 rms spectrum is nearly identical to the rms spectrum which is obtained by comparison of the rms spectra of the Hβ–[O III]λλ4959, 5007 spectral region, corrected and uncorrected for He II λ4686 emission, as described above.

The comparison of the He II λ4686 rms spectrum with the mean Gaussian profile fits to the He II λ4686 line profile indicates that the recovered rms spectrum of the broad He II λ4686
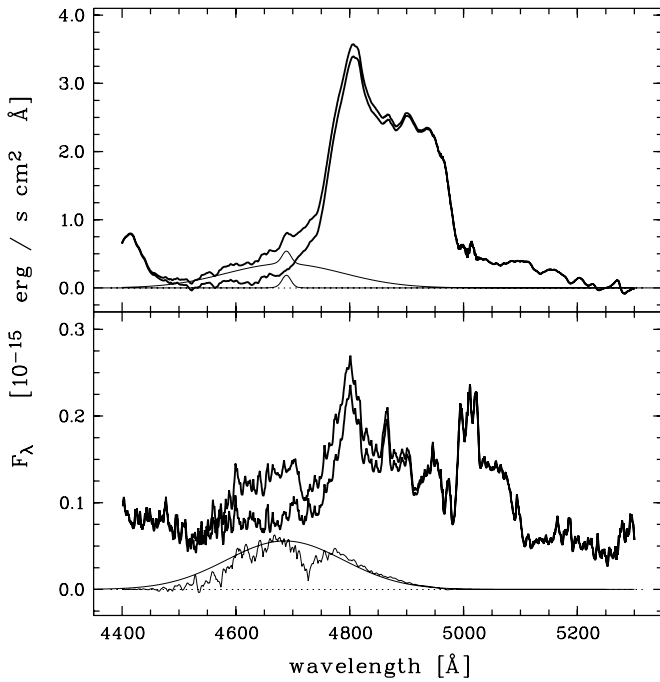
Figure 10. Mean spectrum of the Hβ 4861 emission line is shown (top panel), uncorrected and corrected for contamination by He II λ4686 emission. In addition, the mean narrow and broad He II λ4686 line profile is plotted (thin solid line). In the bottom panel, the corresponding rms spectra of the Hβ λ 4861 line are shown (thick solid lines). The difference between these rms spectra can be associated with the He II λ4686 rms spectrum (thin line). The Gaussian profile shaped rms spectrum for He II λ4686 is shown for comparison (thin solid line).
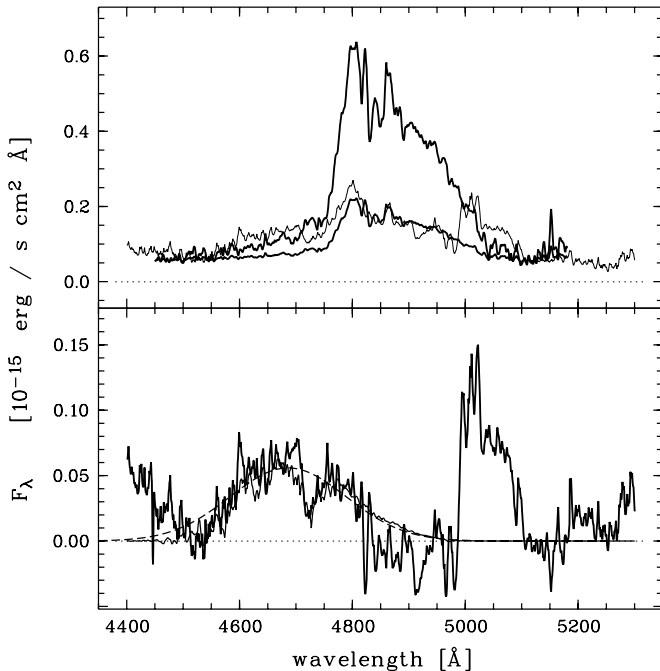
Figure 11. Hβ λ4861 rms spectrum (thin solid line) and the re-binned, as well as the re-binned and scaled Hα λ6563 rms spectrum (thick solid line) are shown (top panel). In the bottom panel, the difference of the Hβ and the re-binned and scaled Hα rms spectra is displayed (thick solid line). For comparison, the He II λ4686 rms spectrum as shown in Figure 10 is shown as thin solid line, as well as the Gaussian profile shaped rms spectrum for He II λ4686 (dashed line).

emission line tends to show less variability in the far blue wing than the mean spectrum and thus the FWHM is smaller. This result is consistent with the properties of the mean and rms spectra of the Balmer emission lines which also show narrower

Table 5
Statistical Properties of the Continuum and Broad Emission-line Variations

Feature (1)	MeanFlux[a] (2)	σ_F [a] (3)	F_{var} (4)	Min (5)	Max (6)
g-band[b]	14.58	0.28	0.050	14.71	14.50
V-band[c]	7.34	0.37	0.051	6.53	7.94
F_λ(5100 Å)[c]	6.63	0.47	0.070	5.65	7.31
Hα λ 6563	2439	128	0.041	2123	2674
Hβ λ 4861	598	32	0.047	538	677
Hγ λ 4340	149	18	0.031	114	171
He II λ4686	88	21	0.155	48	123

Notes.
[a] Integrated line flux in (10^{-15} erg s^{-1} cm^{-2}).
[b] Continuum flux in (mag).
[c] Continuum flux in (10^{-15} erg s^{-1} cm^{-2} Å^{-1}).

profiles in the rms spectra compared with the corresponding mean spectra (Table 4). We used both He II λ4686 rms spectra to measure their FWHM. While the overall shapes of the rms spectra are very similar, the S/N is different. Hence, we used the average of the FWHM, as well as the second moment σ_{line} of the profile. The results are given in Table 4.

4.5. Variability Characteristics

We calculated basic variability parameters to characterize the statistical properties of the observed emission line and continuum variations (Figure 6). The results are presented in Table 5. Column 1 gives the spectral feature. The mean flux and the standard deviation are presented in Columns 2 and 3. The excess variance, F_{var}, in Column 4 is computed as

$$F_{var} = \frac{1}{\overline{F}} \sqrt{\sigma_F^2 - \Delta^2} \qquad (2)$$

with $\overline{F}$ as the mean flux (Column 2), σ_F as the rms of the flux variations, and Δ^2 as the mean square value of the measurement errors (Rodriguez-Pascual et al. 1997). Finally, in Columns 5 and 6, the minimum and maximum fluxes are given for each light curve. The relative variations of the AGN continua (F_λ(5100 Å) and g band) and of the emission lines of Hα, Hβ, and Hγ are of the order of ∼5%. The weak He II λ4686 emission line, however, shows a relative variation of about ∼15%. In spite of the larger uncertainties of the emission-line flux measurements of He II λ4686 these uncertainties are accounted for by the parameter Δ in Equation (2) to calculate the relative variability. There is a trend for stronger relative variations of emission lines with a higher ionization potential of the involved atom. The larger relative variability is also consistent with the results of former variability studies which find that F_{var} of high-ionization lines like He II λ1640 or He II λ4686 are always larger by a factor of about ∼2–3 times than F_{var} for low-ionization lines like Hβ or Hα (e.g., Clavel et al. 1991; Collier et al. 1998; Dietrich et al. 1993, 1998; Korista et al. 1995; O'Brien et al. 1998; Peterson et al. 1991; Reichert et al. 1994; Rodriguez-Pascual et al. 1997; Santos-Lleó et al. 1997; Stirpe et al. 1994; Wanders et al. 1997).

4.6. Time Series Analysis

Generally, AGN monitoring campaigns have focused on the Hβ–[O III]λλ4959, 5007 spectral range because the strong forbidden [O III]λλ4959, 5007 emission lines can be used to establish a robust calibration of the individual spectra. With the large wavelength coverage of this campaign for 3C 390.3, we

Table 6
Results of the Cross-correlation Analysis of the Broad-line Emission of the Balmer Lines Hα, Hβ, Hγ, the Helium Line He IIλ4686,
Using AGN Continuum Variations at $F_\lambda(5100\,\text{Å})$ and the g-band Variations as Driving Continuum

Feature	$F_\lambda(5100\,\text{Å})$			g-band			SPEAR
	$\tau_{\rm cent}$	$\tau_{\rm peak}$	$\rm CCF_{max}$	$\tau_{\rm cent}$	$\tau_{\rm peak}$	$\rm CCF_{max}$	
(1)	(2)	(3)	(4)	(5)	(6)	(7)	(8)
g-band	$0.2^{+1.1}_{-1.1}$	$0.6^{+1.0}_{-1.5}$	0.97 ± 0.01	...	...	...	$0.55^{+1.56}_{-0.45}$
Hα λ 6563	$56.3^{+4.2}_{-4.0}$	$56.5^{+3.5}_{-4.0}$	0.83 ± 0.39	$56.3^{+2.4}_{-6.6}$	$56.5^{+2.0}_{-6.5}$	0.87 ± 0.30	$52.5^{+0.7}_{-0.6}$
Hβ λ 4861	$46.4^{+3.6}_{-3.2}$	$46.5^{+5.0}_{-3.5}$	0.91 ± 0.07	$44.3^{+3.0}_{-3.3}$	$45.0^{+3.0}_{-4.0}$	0.87 ± 0.10	$47.9^{+2.4}_{-4.2}$
Hγ λ 4340	$31.7^{+11.8}_{-10.5}$	$32.0^{+11.5}_{-10.5}$	0.75 ± 0.11	$58.1^{+4.3}_{-6.1}$	$58.0^{+4.5}_{-6.0}$	0.86 ± 0.34	32.1 ± 17.3
He IIλ4686	$24.5^{+5.0}_{-4.7}$	$24.5^{+6.0}_{-5.0}$	0.75 ± 0.11	$22.3^{+6.5}_{-3.8}$	$23.0^{+7.0}_{-4.5}$	0.67 ± 0.13	36.0 ± 5.2

Notes. The centroid of the ICCF has been computed for 80% of the corresponding maximum of the ICCF. The delays calculated with SPEAR are given in Column 8.
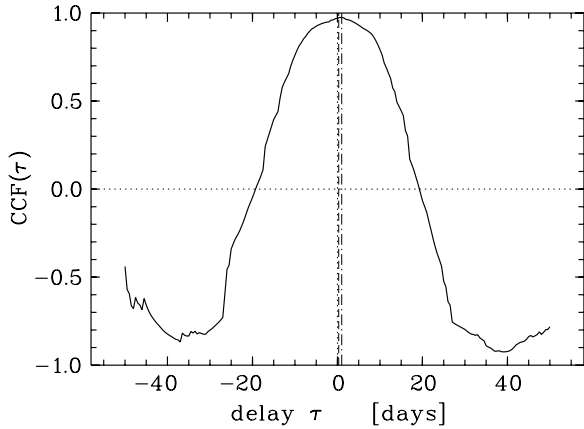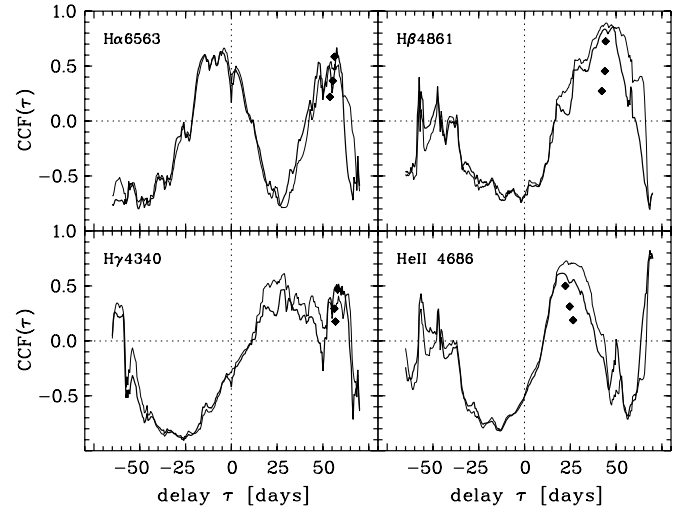

Figure 12. Cross-correlation function of the g-band flux variations with the variable AGN continuum $F_c(5100\,\text{Å})$ as the driving light curve. The location of the centroid ($r \geqslant 0.8\,\rm CCF_{max}$) is shown as dashed line, while the peak of the ICCF is marked by the dashed-dotted line.

Figure 13. Cross-correlation functions of the broad emission lines of Hα, Hβ, Hγ, and He IIλ4686 (thick line) with the g-band variations as the driving light curve. For comparison, the thin lines show the cross-correlation functions using the continuum variations at λ = 5100 Å as driving light curve. The locations of the centroid for a threshold of 30%, 50%, and 80% are shown, respectively, for the ICCF based on the g-band variation (filled diamonds).

are able to study the delayed response of not only Hβ but Hα, Hγ, and He IIλ4686 as well.

To measure the time delay between AGN continuum variations and variable broad-line emission, the continuum light curve is used as the driving light curve with the line emission in response to these variations. To calculate the time delay between the observed variations, we use the interpolation correlation function (ICCF) method (Gaskell & Peterson 1987; White & Peterson 1994; Peterson et al. 1998, 2004). For this monitoring campaign, we derived an AGN continuum light curve from the power-law continuum fits at λ = 5100 Å as well as the g-band light curve.

First, we selected an appropriate continuum light curve. Since the g-band flux contains variable broad Hβ emission in addition to the AGN continuum, we studied the impact of the broad Hβ line emission on the g-band variations. The contribution of the host galaxy can be assumed to be constant. The g-band light curve and the $F_\lambda(5100\,\text{Å})$ light curve (Figure 6) are cross correlated using the ICCF method with $F_\lambda(5100\,\text{Å})$ as the driving light curve. The resulting CCF is shown in Figure 12. Close inspection of this CCF shows that the g-band light curve is delayed with respect to the $F_\lambda(5100\,\text{Å})$ variations by $\tau_{\rm cent} = (0.2 \pm 1.1)$ days and $\tau_{\rm peak} = (0.6 \pm 1.2)$ days, respectively (Table 6). Within the uncertainties, the $F_\lambda(5100\,\text{Å})$ variations and the g-band variations are simultaneous and the detected small delay can be neglected. It is reasonable to attribute this hint of a delay to the variable broad Hβ emission which is part of the g-band flux. Since the scatter in the g-band fluxes is

much smaller than in the $F_\lambda(5100\,\text{Å})$ continuum light curve, we selected the g-band variations as the driving continuum in the subsequent cross-correlation analysis. For comparison, we also provide the cross-correlation results using $F_\lambda(5100\,\text{Å})$ as the driving continuum light curve (Table 6). The cross-correlation functions (ICCFs) for the broad emission lines are displayed in Figure 13. The ICCFs show some asymmetric shape and the region around the peak has some structure as well.

To quantify the uncertainties in the time delay measurements, we employ the model-independent Monte Carlo FR/RSS method (Peterson et al. 1998), including modifications described by Peterson et al. (2004). For each single realization of the method, random subset sampling (RSS) is applied in which a light curve with N data points is randomly sampled N times without regard to the previous selection of each point. Flux randomization (FR), in which a random Gaussian deviation, based on the associated error, is then applied to each of the selected N points. This FR/RSS-altered subset of data points is then cross-correlated as though it were real data. The peak of the cross-correlation function, $r_{\rm max}$, which occurs at a time lag $\tau_{\rm peak}$, is determined, as is the centroid, $\tau_{\rm cent}$. A cross-correlation peak distribution (CCPD) for $\tau_{\rm peak}$ and a cross-correlation centroid distribution (CCCD) for $\tau_{\rm cent}$ are built with a large number

Table 7
Location of the Blue and Red Peaks, as well as of a Red Feature in the Broad-line Profiles of the Hα, Hβ, and Hγ Emission, if Detectable

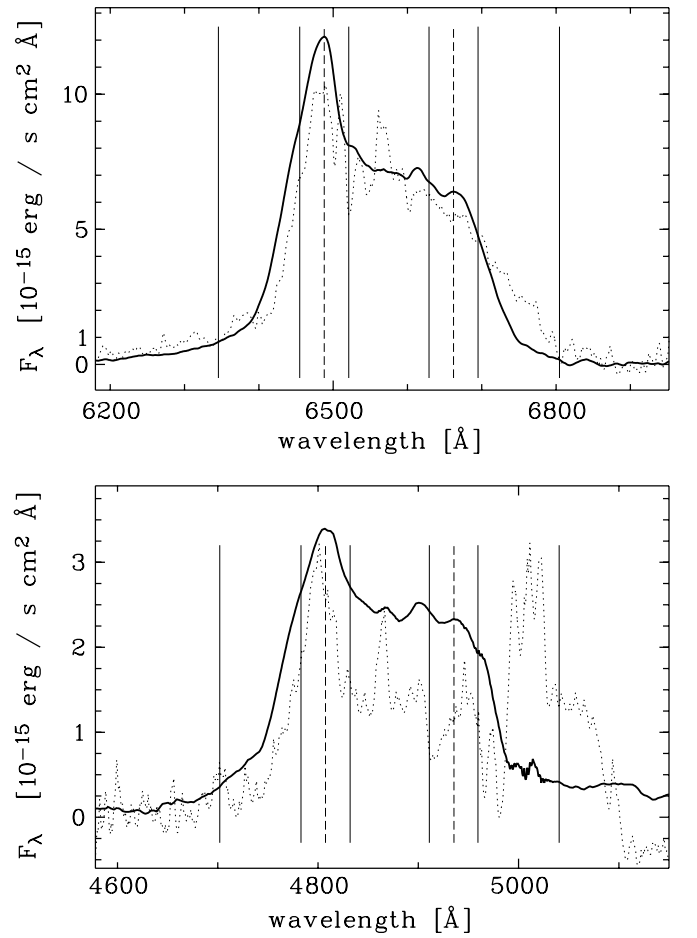|	Mean Spectra					
Feature	Blue Peak		Red Peak		Red Feature	
	(Å)	(km s^{-1})	(Å)	(km s^{-1})	(Å)	(km s^{-1})
(1)	(2)	(3)	(4)	(5)	(6)	(7)
Hα λ 6563	6488.3 ± 1.0	−3413 ± 41	6662.1 ± 0.0	+4538 ± 54	6613.0 ± 1.0	+2292 ± 38
Hβ λ 4861	4807.4 ± 1.0	−3324 ± 49	4935.3 ± 0.0	+4563 ± 68	4901.6 ± 1.0	+2485 ± 42
Hγ λ 4340	4287.6 ± 1.0	−3650 ± 69	4409.7 ± 1.5	+4783 ± 104	. . .	. . .
	rms Spectra					
Feature	Blue Peak		Red Peak		Red Feature	
	(Å)	(km s^{-1})	(Å)	(km s^{-1})	(Å)	(km s^{-1})
Hα λ 6563	6483.5 ± 2.0	−3622 ± 91	6665.9 ± 2.0	+4711 ± 228	6619.3 ± 4.0	+2582 ± 183
Hβ λ 4861	4801.5 ± 3.0	−3689 ± 185	4945.8 ± 4.0	+5210 ± 247	4897.1 ± 6.0	+2207 ± 370
Hγ λ 4340	4293.0 ± 10.0	−3277 ± 690	4402.0 ± 6.0	+4251 ± 415	. . .	. . .

($N \simeq 10{,}000$) of Monte Carlo realizations. We take the average value of the CCPD to be τ_{peak} and the average of the CCCD to be τ_{cent}. To calculate the uncertainties $\Delta\tau_{up}$ and $\Delta\tau_{low}$ we assume that 15.87% of the cross-correlation centroid realizations have values $\tau > \tau_{cent}+\Delta\tau_{up}$ and 15.87% have values $\tau < \tau_{cent}-\Delta\tau_{low}$, with analog estimated uncertainties for τ_{peak}. These definitions of the uncertainty correspond to $\pm 1\sigma$ for a Gaussian distribution.

4.6.1. Velocity-dependent Broad Emission-line Variations

While the variability characteristics of the integrated broad-line flux can be used to infer the size of the BLR, the analysis of the response of different parts of the broad emission-line profile, e.g., the line core, and the profile wings, yield information on the dominant gas motion, i.e., the kinematics of the broad emission-line gas (e.g., Blandford & McKee 1982; Horne et al. 2004). Previous investigations of 3C 390.3 have found that the profile wings vary in phase (Dietrich et al. 1998; Popovic et al. 2011; Sergeev et al. 2002; Shapovalova et al. 2010) which strongly favors orbital motion, i.e., virial motion dominates the gas kinematics. This is also supported by accretion disk models to describe the double-peaked Balmer emission-line profiles (e.g., Eracleous & Halpern 1994; Flohic & Eracleous 2008). Recently, results for several AGNs have been presented (Denney et al. 2009a; Bentz et al. 2009b) which indicate a more complex picture with signatures for orbital motion as well as for radial motions. In addition, for Arp 151 the analysis of spectroscopically resolved broad emission-line results into velocity-delay maps which indicate the presence of substructures like orbiting hot spots (Bentz et al. 2010a).

As in former studies of 3C 390.3, we extracted light curves for different parts of the broad emission-line profile. For better comparison with prior studies (e.g., Dietrich et al. 1998; Gezari et al. 2007; Shapovalova et al. 2010), the width and placement of those regions are motivated by the location and the widths of the blue and red peaks in the double-peaked line profile.

In Table 7, the location of the blue peak and red peak for the Hα, Hβ, and Hγ emission-line profiles are given. Within ∼100 km s^{-1} both peaks are at similar velocities. Based on the mean line profiles (Figure 9), the width of the peaks amounts to FWHM ≃ 50 Å and FWHM ≃ 70 Å for Hβ and Hα, respectively. We investigated the profiles of the Hα and Hβ emission lines only because the Hγ emission line is too weak and He IIλ4686 is best represented by a single Gaussian profile. We extracted the light curves of the blue and red peaks for a 3000 km s^{-1}

Figure 14. Location of the extraction windows for the blue and red wings, the blue and red peaks, and the center of the broad-line profiles of the Hα (top panel) and Hβ (bottom panel) emission lines using the mean spectrum (solid line) and the rms spectrum (dotted line, scaled by a factor of 20). The long dashed line indicates the measured location of the blue and red peaks.

wide region. In Figure 14 the boundaries of the blue and red wings, the blue and red peaks, and the line center are shown. For comparison the location of those profile sections are given in Table 8 which were used by Gezari et al. (2007). The errors for the extracted light curves were determined following the same approach as for the integrated emission-line fluxes.

Table 8
Range of the Line Profile Regions to Extract Light Curves for the Profile Wings, the Line Center, and the
Blue and Read Peaks in the Broad Emission-Line Profiles of the Hα and Hβ Lines

Feature	Hα λ 6563	Hβ λ 4861
(1)	(2)	(3)
Blue wing	6345.5–6455.0 Å	4702.0–4783.0 Å
	−9916 km s^{-1} to −4916 km s^{-1}	−9819 km s^{-1} to −4819 km s^{-1}
	(−12300 km s^{-1} to −4500 km s^{-1})	
Blue peak	6455.0–6521.0 Å	4783.0–4832.0 Å
	−4916 km s^{-1} to −1916 km s^{-1}	−4819 km s^{-1} to −1819 km s^{-1}
	(−4500 km s^{-1} to −1700 km s^{-1})	
Center	6521.0–6629.0 Å	4832.0–4911.0 Å
	−1916 km s^{-1} to +3032 km s^{-1}	−1819 km s^{-1} to +3063 km s^{-1}
	(−1700 km s^{-1} to +3300 km s^{-1})	
Red peak	6629.0–6695.0 Å	4911.0–4959.5 Å
	+3032 km s^{-1} to +6032 km s^{-1}	+3063 km s^{-1} to +6063 km s^{-1}
	(+3300 km s^{-1} to +5900 km s^{-1})	
Red wing	6695.0–6804.5 Å	4959.5–5040.5 Å
	+6032 km s^{-1} to +11032 km s^{-1}	+6063 km s^{-1} to +11063 km s^{-1}
	(+5900 km s^{-1} to +15000 km s^{-1})	

Note. In brackets the velocity ranges are given which are used by Gezari et al. (2007).

Table 9
Results of the Cross-correlation Analysis of the Wings, the Center, and the Blue and Red Peaks of the Broad Balmer Lines Hα and Hβ
Using AGN Continuum Variations at F_λ(5100 Å) and the g-band Variations as Driving Continuum

Feature	F_λ(5100 Å)			g-band		
	$\tau_{\rm cent}$	$\tau_{\rm peak}$	CCF$_{\rm max}$	$\tau_{\rm cent}$	$\tau_{\rm peak}$	CCF$_{\rm max}$
(1)	(2)	(3)	(4)	(5)	(6)	(7)
Hα blue wing	$57.5^{+4.7}_{-5.5}$	$58.0^{+5.0}_{-4.5}$	0.88 ± 0.47	$55.9^{+4.0}_{-5.6}$	$57.0^{+3.0}_{-5.0}$	0.92 ± 0.59
Hα blue peak	$54.3^{+6.2}_{-4.4}$	$56.5^{+4.5}_{-5.0}$	0.84 ± 0.49	$53.2^{+5.1}_{-5.0}$	$55.5^{+3.0}_{-7.0}$	0.85 ± 0.56
Hα center	$54.5^{+6.0}_{-4.2}$	$56.5^{+4.5}_{-4.5}$	0.82 ± 0.41	$53.5^{+4.9}_{-4.9}$	$56.0^{+2.5}_{-7.0}$	0.85 ± 0.73
Hα red peak	$54.1^{+6.7}_{-4.4}$	$56.5^{+4.5}_{-6.5}$	0.85 ± 0.26	$52.7^{+6.3}_{-5.5}$	$55.0^{+4.0}_{-7.5}$	0.86 ± 0.20
Hα red wing	$56.8^{+6.8}_{-7.2}$	$57.5^{+6.0}_{-8.0}$	0.89 ± 0.40	$49.9^{+10.5}_{-4.4}$	$51.0^{+10.5}_{-4.0}$	0.95 ± 1.28
Hα blue vs. red wing	$-3.4^{+7.4}_{-6.8}$	$-2.5^{+7.5}_{-8.0}$	0.64 ± 0.10			
Hα blue vs. red peak	$0.2^{+3.9}_{-3.6}$	$0.0^{+1.0}_{-0.5}$	0.67 ± 0.10			
Hβ blue wing	$49.6^{+12.4}_{-11.0}$	$52.0^{+10.0}_{-16.0}$	0.84 ± 0.34	$48.4^{+11.3}_{-8.8}$	$49.5^{+11.0}_{-10.0}$	0.84 ± 0.16
Hβ blue peak	$48.0^{+13.3}_{-9.7}$	$51.0^{+10.5}_{-14.5}$	0.86 ± 0.71	$47.2^{+12.1}_{-9.1}$	$49.0^{+11.0}_{-11.5}$	0.85 ± 0.27
Hβ center	$49.6^{+12.4}_{-13.7}$	$53.0^{+9.0}_{-19.0}$	0.85 ± 0.56	$49.0^{+11.4}_{-10.4}$	$50.5^{+10.5}_{-12.0}$	0.84 ± 0.19
Hβ red peak	$51.6^{+7.0}_{-7.9}$	$54.5^{+4.5}_{-11.0}$	0.80 ± 0.19	$53.1^{+7.1}_{-9.4}$	$54.5^{+6.0}_{-10.0}$	0.86 ± 0.74
Hβ red wing	$54.4^{+6.0}_{-10.3}$	$56.0^{+4.5}_{-11.5}$	0.81 ± 0.35	$56.3^{+5.9}_{-9.6}$	$57.0^{+5.5}_{-8.0}$	0.91 ± 0.71
Hβ blue vs. red wing	$2.9^{+13.4}_{-18.5}$	$3.0^{+18.0}_{-22.0}$	0.47 ± 0.10			
Hβ blue vs. red peak	$1.0^{+8.8}_{-9.8}$	$0.0^{+10.0}_{-10.0}$	0.50 ± 0.11			

**Note.** The centroid of the ICCF has been computed for 80% of the corresponding maximum of the ICCF.

Next, the Hα and Hβ line profile section variations are cross-correlated with the g-band light curve, as well as with the AGN continuum F_λ(5100 Å). In Figure 15, the corresponding ICCF(τ) are shown. While for Hα the light curves of the blue wings, the blue and red peaks, and of the line center result into ICCFs with well-defined structures, the light curve of the red wing of the broad Hα line profile results in an ICCF which provides merely an indication for a possible delay (Figure 15). For the Hβ line profile the ICCFs are broad and in the case of the red wing for Hβ there is only a weak indication for a marginally defined peak (Figure 15).

The location of the centroid, the peak, and the uncertainties in the ICCFs for the wings, the peaks, and the line center of the Hα and Hβ emission lines are determined using the technique described above (Section 4.3) and the results are given in Table 9. As can be seen already in Figure 15, the blue and red peaks of the Hα line and of the Hβ line vary basically with the same

time delay relative to the continuum variations, consistent with the model that the hydrogen Balmer line emission originates in a rotating disk (e.g., Eracleous & Halpern 1994; Flohic & Eracleous 2008). Within the uncertainties, there is also no delay of the profile wings with respect to the peaks or the center of the line profile. To test this result, we also applied the time series analysis to the variations of the blue and red wings and the blue and red peaks to eliminate uncertainties which are introduced by the continuum light curves. The corresponding ICCFs for the Hα and Hβ lines are displayed in Figures 16. Within the uncertainties we detect no time delay between the variations of the blue and red peaks and wings (Table 9).

4.7. Stochastic Process Estimation for AGN Reverberation

Generally, the time delay between continuum and broad emission-line flux variations is determined by calculating
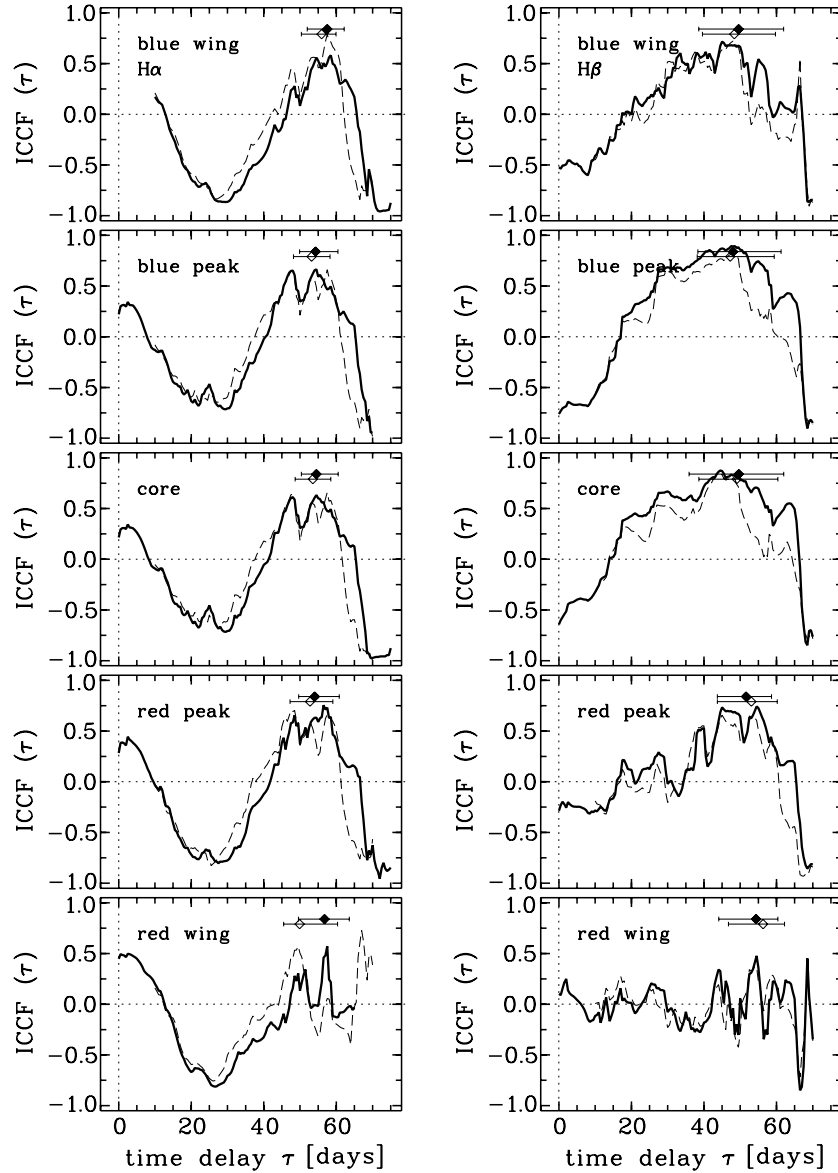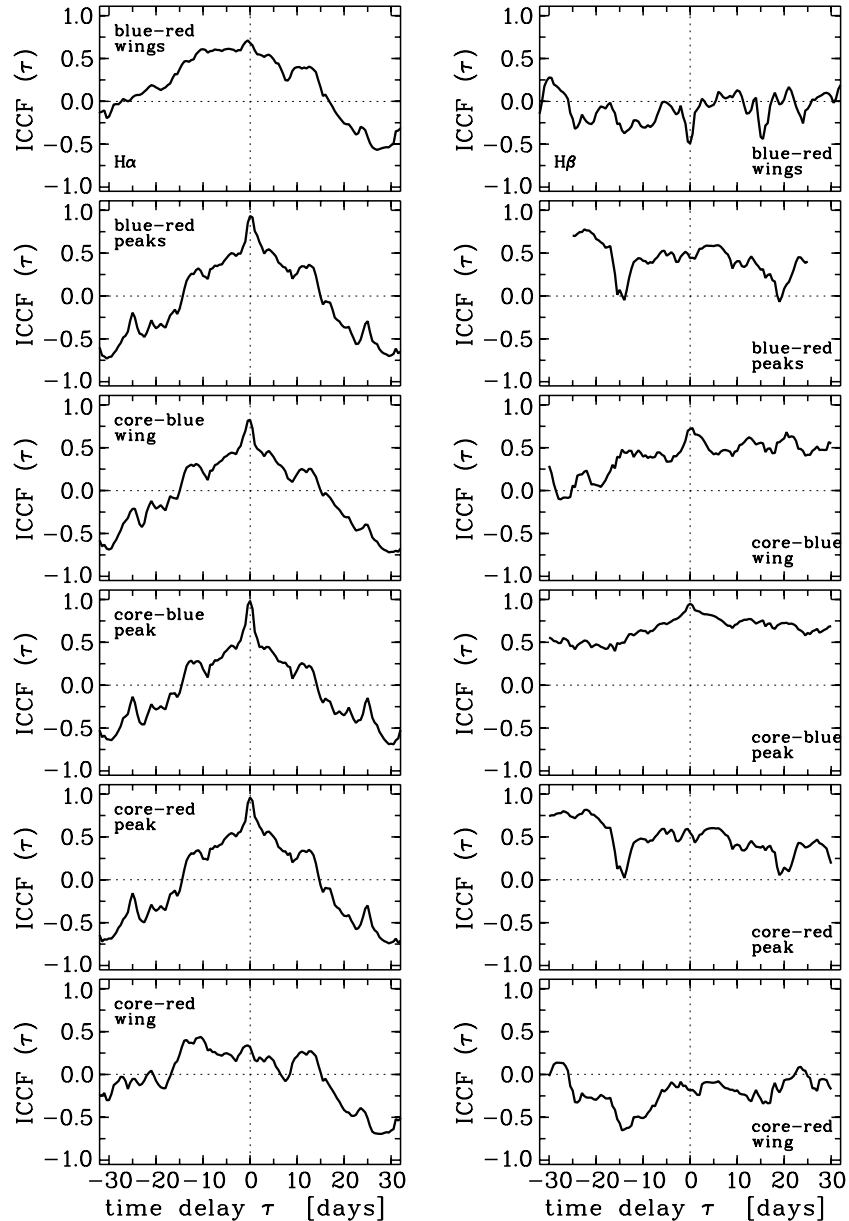
Figure 15. Cross-correlation functions using the AGN continuum $F_\lambda(5100\,\text{Å})$ as driver light curve (solid line) for the blue wing, blue peak, line center, red peak, and red wing (top to bottom) of the broad Hα line profile (on the left) and of the broad Hβ line profile (on the right). The ICCFs obtained with the g-band variations as driving continuum are shown as dashed line. The location of the centroid, based on a threshold of 80% of ICCF$_{\max}$ and the corresponding uncertainty, is shown as filled diamonds ($F_\lambda(5100\,\text{Å})$) and open diamonds ($g$ band), respectively.

cross-correlation functions. However, for a better specification of the possible impact of gaps in the temporal coverage of the light curves, an alternative approach has been recently suggested by Zu et al. (2011) and applied by Grier et al. (2012) to the measured variability of the NLS1 galaxy Mkn 335. This method to analyze irregularly sampled light curves with a more statistical approach was developed by Press et al. (1992) and Rybicki & Press (1992). They assumed that an irregularly sampled light curve can be treated as a damped random walk process with a specific amplitude $\hat{\sigma}$ and an exponential damping timescale τ_d. In recent years it has been shown that quasar light curves can be, indeed, well described with this approach (Kelly et al. 2009; Zu et al. 2012) and furthermore that the amplitude $\hat{\sigma}$ and damping timescale τ_d for quasar variability are found in a well-defined region of the $\hat{\sigma} - \tau_d$ space (Kozłowski et al. 2010; MacLeod et al. 2010). Recently, Mushotzky et al. (2011), however, have shown using *Kepler* data for four AGNs, that the variability of all AGNs cannot be described with the random walk approach

but that individual AGNs have intrinsically different variability characteristics.

To investigate also AGN variability data and in particular the impact of gaps in the temporal sampling in AGN light curves, Zu et al. (2011) have modified this statistical approach. We used their method of Stochastic Process Estimation for AGN Reverberation (SPEAR) as presented by Zu et al. (2011) to investigate the variations of 3C 390.3 (Figure 6). First, we used the g-band variation and the $F_\lambda(5100\,\text{Å})$ variability to test whether the SPEAR results are consistent with our cross-correlation results (Table 6). We started with an amplitude of $\hat{\sigma} = 0.05$ and a damping timescale of $\tau_d = 60$ days. With the g-band variations as a driver light curve (because of its much smaller errors than the $F_\lambda(5100\,\text{Å})$ light curve), we find using SPEAR a delay of $\tau = 0.55^{+1.56}_{-0.45}$ days which is consistent with the cross-correlation result.

Next, we used the g-band light curve as the driver to recover the time delays of the Hα, Hβ, Hγ, and He IIλ4686 variations.

Figure 16. Cross-correlation functions for Hα (left panels) and for Hβ (right panels) correlating the blue and red wings, as well as the blue and red peaks of the line profiles directly, with the blue light curve as driver and the red light curve in response (top two panels). The following panels show the ICCFs using the variations of the line center as driving light curve and the profile wings and peaks in response.

Using SPEAR, we computed time delays for the strong Balmer lines Hα and Hβ which are basically identical within the errors to the cross-correlation based delays. In the case of the Hγ and He II λ4686 emission lines, however, the delays determined with SPEAR and based on the cross-correlation analysis show some differences. The time delays of the Balmer lines Hα, Hβ, and Hγ derived with SPEAR are consistent with those of the ICCF analysis using F_λ(5100 Å) as the driving continuum. However, for the He II λ4686 emission lines the delays are just consistent within the 1σ errors. The time delay of the Hγ variations based on the g-band light curve as the driver continuum and the SPEAR result differ by nearly a factor of two (Table 6). Furthermore, due to the larger uncertainties of the flux measurements for the Hγ and He II λ4686 emission lines, SPEAR needed to be restricted to a narrow range of allowed time delays to avoid spurious delays at τ ≃ 120 days, which is longer than the period covered by the experiment.

SPEAR treats large gaps in the temporal coverage of a light curve in a statistically based approach and also follows the impact on the uncertainty of the time delay. However, in the case of the study of 3C 390.3 with no large gaps in the light curve, we applied SPEAR predominantly to compare the results with those of the ICCF analysis and the results of both methods do well agree. Hence, we used the results of the ICCF analysis in the following for consistency with former variability investigations which allows an easier comparison with those results.

4.8. Black Hole Mass and Eddington Ratio

4.8.1. Black Hole Mass Estimates

To determine the mass of the black hole in the center of 3C 390.3, we assumed that the line-emitting gas is bound, i.e., that the virial theorem can be applied. This approach is well motivated by the results of the fitting of the double-peaked
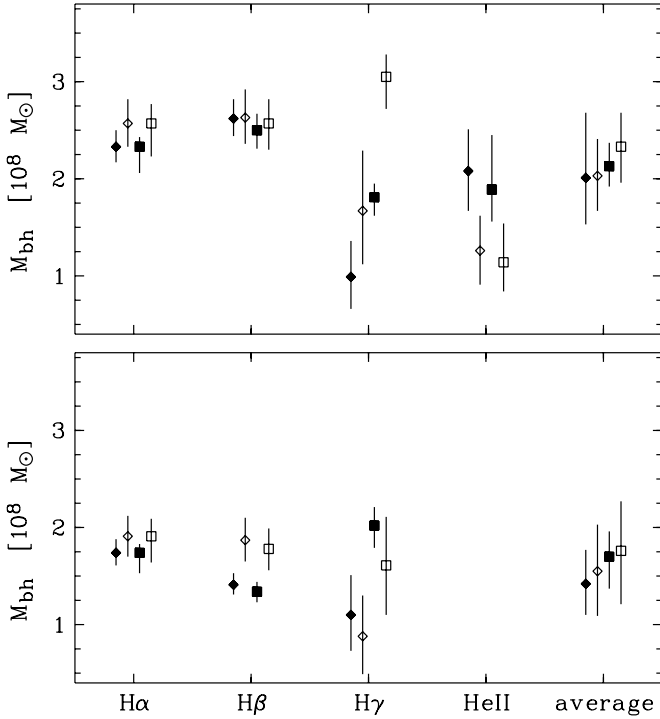
Figure 17. Comparison of the black hole mass estimates that are based on the measured time delay for the Balmer lines and the helium He IIλ4686 line using the second moment σ_{line} of the line profiles (top panel) and the blue–red peak separation (bottom panel). The black hole masses based on the mean line profiles and the blue–red peak separations are shown as filled symbols while the rms spectra results are given by the open symbols. The diamonds represent the black hole masses using the AGN continuum F_λ(5100 Å) to determine the time delay while the boxes display the results using the g-band variations.

Table 10
Estimates of the Black Hole Virial Product M_{bh}^{vir}, Based on the Balmer and Helium Line Profile Properties (σ_{line} and Separation of the Blue and Red Peaks in the Double-peaked Profiles) and the Time Delays τ_{cent} (80% Threshold) of the Broad Emission-line Flux Variations

Virial Black Hole Product M_{bh}^{vir} in $10^8\,M_\odot$				
Using σ_{line} of the line profiles				
Feature	F_λ(5100 Å)		g-band	
	M_{bh}^{vir}(mean)	M_{bh}^{vir}(rms)	M_{bh}^{vir}(mean)	M_{bh}^{vir}(rms)
(1)	(2)	(3)	(4)	(5)
Hα λ 6563	$2.33^{+0.17}_{-0.16}$	$2.57^{+0.25}_{-0.24}$	$2.33^{+0.10}_{-0.27}$	$2.57^{+0.20}_{-0.34}$
Hβ λ 4861	$2.62^{+0.20}_{-0.18}$	$2.69^{+0.29}_{-0.27}$	$2.50^{+0.17}_{-0.19}$	$2.57^{+0.25}_{-0.27}$
Hγ λ 4340	$0.99^{+0.37}_{-0.33}$	$1.67^{+0.62}_{-0.55}$	$1.81^{+0.14}_{-0.19}$	$3.05^{+0.23}_{-0.33}$
He IIλ4686	$2.08^{+0.43}_{-0.41}$	$1.26^{+0.36}_{-0.35}$	$1.89^{+0.56}_{-0.33}$	$1.14^{+0.40}_{-0.30}$
Average	$2.01^{+0.67}_{-0.48}$	$2.05^{+0.38}_{-0.36}$	$2.13^{+0.24}_{-0.21}$	$2.33^{+0.35}_{-0.37}$
Using the separation of the blue and red peak				
Feature	F_λ(5100 Å)		g-band	
	M_{bh}^{vir}(mean)	M_{bh}^{vir}(rms)	M_{bh}^{vir}(mean)	M_{bh}^{vir}(rms)
(1)	(2)	(3)	(4)	(5)
Hα λ 6563	$1.74^{+0.14}_{-0.13}$	$1.91^{+0.21}_{-0.21}$	$1.74^{+0.09}_{-0.21}$	$1.91^{+0.18}_{-0.27}$
Hβ λ 4861	$1.41^{+0.12}_{-0.10}$	$1.87^{+0.23}_{-0.22}$	$1.34^{+0.10}_{-0.11}$	$1.78^{+0.21}_{-0.22}$
Hγ λ 4340	$1.10^{+0.41}_{-0.37}$	$0.88^{+0.42}_{-0.39}$	$2.02^{+0.19}_{-0.23}$	$1.61^{+0.50}_{-0.51}$
Average	$1.42^{+0.35}_{-0.32}$	$1.55^{+0.48}_{-0.46}$	$1.70^{+0.26}_{-0.33}$	$1.77^{+0.29}_{-0.31}$

emission-line profiles of 3C 390.3 with an elliptical disk model (Flohic & Eracleous 2008). In addition, for several AGNs it has been possible to measure the time delay of additional broad emission-line flux variations. These studies consistently show that emission lines with higher ionization energies show shorter time delays, in keeping with the observed ionization stratification of the BLR and their closer locations to the central continuum source (Bentz et al. 2009a; Kollatschny 2003; Onken & Peterson 2002; Peterson & Wandel 1999, 2000). Together with broader emission-line profile widths, these results provide strong support that the gas is in gravitationally bound motion. The virial mass of the black hole is given by

$$M_{bh}^{vir} = f\, \frac{c\,\tau\,\Delta v^2}{G} \qquad (3)$$

with $c\,\tau$ as the size of the broad emission-line region, Δv which is associated with the line profile width, and G as the gravitational constant. The factor f depends on the geometry, kinematics, and the orientation of the line-emitting region. It has been shown by Onken et al. (2004) that the average of f amounts to $\langle f \rangle = 5.5$ when the virial black hole mass, based on a rms spectrum profile width, is calibrated to the M_{bh}–σ_* relation for quiescent galaxies (e.g., Tremaine et al. 2002; Gültekin et al. 2009, 2011). In the following, we calculate the pure virial product, i.e., we will assume $f = 1.0$ because in the case of 3C 390.3 and the successful accretion disk models $v_{obs} = v_{intr} \times \sin i$ can be used to derive the intrinsic velocity, v_{intr}, of the gas.

$$M_{bh}^{vir} = 1.951 \times 10^5 \left(\frac{\tau}{\text{days}} \right) \left(\frac{\sigma_{line}}{1000\,\text{km s}^{-1}} \right)^2 \, M_\odot. \qquad (4)$$

Using the second moment of the emission-line profiles σ_{line} (cf. Peterson et al. 2004) for the mean and rms spectra (Table 4) and the measured time delay of the broad emission-line flux response to continuum variations, given by τ_{cent} (Table 6), derived from a threshold of 80% of the maximum of the ICCF, we calculated the virial black hole mass using Equation (4). The results are presented in Table 10. For comparison we estimated black hole masses for the individual emission lines using σ_{line} from the the mean and the rms spectra and the time delay which we derived using the AGN continuum variations of F_λ(5100 Å) and of the g band as well (Table 6). We find that within the uncertainties, the virial mass, M_{bh}^{vir}, of the black hole of 3C 390.3, based on the mean emission-line profiles, is in the range of $1.0 \times 10^8\,M_\odot$ to $2.6 \times 10^8\,M_\odot$ based on the properties of the mean profiles of the Balmer lines and the He IIλ4686 emission line, independent of the continuum used (Figure 17 and Table 10). However, if only the strong Balmer emission lines Hα and Hβ are considered because the uncertainties for the Hγ and He IIλ4686 emission lines are larger, the virial products are in better agreement, $2.3 \times 10^8\,M_\odot$ to $2.6 \times 10^8\,M_\odot$. The rms spectra yield results which are consistent with the mean spectrum with virial black hole masses of $1.1 \times 10^8\,M_\odot$ to $3.0 \times 10^8\,M_\odot$ (Table 10) and the strong Balmer emission lines Hα and Hβ yield black hole mass estimates of about $\sim 2.6 \times 10^8\,M_\odot$. Since, the rms spectrum represents the actually variable part of the emission-line profile, we conclude that the virial product of the black hole of 3C 390.3, based on the strong Balmer emission lines Hα and Hβ is $M_{bh}^{vir}(3C\,390.3) = (2.60^{+0.23}_{-0.31}) \times 10^8\,M_\odot$.

To estimate the black hole mass M_{bh} using RM studies, it is still necessary to specify the factor f in Equation (3) which depends on the not well-constrained geometry and kinematics of the gas, as well as on the orientation of the line-emitting region. While it is generally assumed that this factor f is of the order of unity, it has been pointed out that a small inclination of the line-emitting region can result in a significant underestimation of

the black hole mass (e.g., Collin et al. 2006) if the gas motions are almost entirely in the disk plane with little motion in the polar direction. In contrast to almost all AGNs monitored so far, the BLRG 3C 390.3 is unique since it is the only radio-loud AGN with extended double-lobed radio emission (Leahy & Perley 1995) whose variability has been studied in detail. This allows us to estimate the impact of the inclination i of the line-emitting region on the black hole mass measurement and hence the factor f, assuming pure disk motion of the gas. Based on very long baseline interferometry observations, Alef et al. (1988) reported indications for super-luminal motion for 3C 390.3. Further radio observations and a detailed analysis provided information on the inclination i of the axis of the radio emission in 3C 390.3 (Alef et al. 1994, 1998), which was found to be $i = 28°^{+5°}_{-9°}$. The inclination of the radio axis of 3C 390.3 has been also estimated based on X-ray observations (Eracleous et al. 1996). They successfully modeled the resolved Fe Kα line emission with X-ray reprocessing in a cool, dense disk of gas at an inclination of $i \simeq 26°$. A third way to estimate the inclination of the disk-like line-emitting region is provided by fitting the double-peaked profile. Using a relativistic Keplerian disk, Eracleous & Halpern (1994) derived an inclination angle of $i = 26°^{+4°}_{-2°}$. Recently, Flohic & Eracleous (2008) analyzed the variations of the double-peaked profile shape of Hα for Arp 102B and 3C 390.3. They found that the best disk models for 3C 390.3 strongly indicate an inclination angle of $i = 27° \pm 2°$.

In a simple model of an accretion disk as the dominant source of the observed double-peaked emission-line profile, the observed velocity is actually $v_{obs} = v_{intr} \times \sin i$. Assuming an inclination angle of $i = 27° \pm 2°$ this implies a correction factor of $f = 4.85^{+0.75}_{-0.60}$. Within the uncertainties, this factor is consistent with $\langle f \rangle = 5.5$, determined by Onken et al. (2004) and $\langle f \rangle = 5.25$ by Gültekin et al. (2009) which were determined by comparing the reverberation-based black hole masses with the masses determined using the M–σ relation, with the stellar velocity dispersion σ based on stellar or gas dynamics of the host galaxy's bulge. Applying the correction due to the measured inclination of the accretion disk, the black hole mass of 3C 390.3 based on the Hα and Hβ rms spectrum profile properties and τ_{cent} yields $M_{bh}(3C 390.3) = (1.26^{+0.21}_{-0.16}) \times 10^9 M_\odot$.

Accretion disk models have been shown to be successful in explaining the observed profiles and even profile variations over longer timescales for 3C 390.3, Thus, the typical velocity of the line-emitting gas can be associated with the location of the blue and red peaks of the double-peaked emission-line profile, i.e., the location in velocity space of the dominant part of the line-emitting gas. Using the separation of the blue and red peaks of the Balmer emission-line profiles as Δv, we estimated the virial product using Equation (4) and τ_{cent} (80% threshold level). The derived black hole masses are given in Table 10. Based on the Balmer emission lines Hα, Hβ, and Hγ we find virial black hole masses in the range of $1.1 \times 10^8 \lesssim M_{bh} \lesssim 2.0 \times 10^8 M_\odot$ using the mean emission-line profiles and $0.9 \times 10^8 \lesssim M_{bh} \lesssim 1.9 \times 10^8 M_\odot$ based on the rms spectra (Figure 17 and Table 10). However, this wide range is caused by the Hγ-based results which have a larger uncertainty than the black hole mass estimates obtained from the strong Hα and Hβ emission lines which are consistent within the errors. Since the rms spectrum represents the actual variable part of the emission-line gas, we calculated the average virial black hole mass which is based on the rms spectra of the Balmer emission lines Hα, Hβ, and Hγ. We find a virial black hole mass of $M_{bh}^{vir} = (1.77^{+0.29}_{-0.31}) \times 10^8 M_\odot$. Together with the correction

factor $f = 4.85^{+0.75}_{-0.60}$ which is given by the inclination of the accretion disk, we find for the black hole mass for 3C 390.3 a value of $M_{bh} = 0.86^{+0.19}_{-0.18} \times 10^9 M_\odot$.

4.8.2. Eddington Ratio

Using the black hole mass estimates based on the broad Balmer and emission-line profiles in the rms spectrum and the optical continuum luminosity of 3C 390.3 at $\lambda = 5100$ Å, we computed the Eddington ratio L_{bol}/L_{edd}. The value of the conversion factor f_L between the monochromatic luminosity and the bolometric luminosity ($L_{bol} = f_L \times \lambda F_\lambda(5100)$) is still debated in the literature (e.g., Elvis et al. 1994; Laor 2000; Netzer 2003; Richards et al. 2006). Recently, Marconi et al. (2008) even suggested a luminosity-dependent correction factor f_L, due to radiation pressure effects. We assumed that the bolometric luminosity is given by $L_{bol} = 9.74 \times \lambda L_\lambda(5100$ Å$)$ (Vestergaard 2004). We find $L_{bol} = 2.22 \times 10^{45}$ erg s^{-1}. To calculate the Eddington luminosity L_{edd}, we assumed that the gas is a mixture of hydrogen and helium ($\mu = 1.15$), i.e., $L_{edd} = 1.45 \times 10^{38} M_{bh} / M_\odot$ erg s^{-1}. The derived Eddington ratio L_{bol}/L_{edd} for 3C 390.3, based on this monitoring campaign, amounts to $L_{bol}/L_{edd} = 0.018^{+0.006}_{-0.005}$. This low Eddington ratio is typical for radio-loud AGNs like 3C 390.3 (e.g., Boroson & Green 1992; Boroson 2002).

5. DISCUSSION

5.1. Times Series Analysis and the Size of the BLR

Recently, results of studies on the long-term variability properties of 3C 390.3 have been presented by Sergeev et al. (2002, 2011) and Shapovalova et al. (2010). In two studies, Sergeev et al. (2002, 2011) investigated the correlated variations of the optical continuum and the response of the broad Hβ emission-line flux for the years 1992–2000 and 2000–2007, respectively. In both studies they found that the Hβ variations are delayed by $\tau(H\beta) = 82^{+12}_{-10}$ days (1992–2000) and $\tau(H\beta) = 94 \pm 6$ days (2000–2007) and for Hα delays of $\tau(H\alpha) = 162^{+32}_{-15}$ days (1992–2000) and $\tau(H\alpha) = 174 \pm 16$ days (2000–2007) were determined. A comparable result was found by Shapovalova et al. (2010) who studied the optical variations for 3C 390.3 from 1995 to 2007. They report that the variations of the broad Hβ and Hα emission-line flux are delayed by $\tau(H\beta) = 96^{+28}_{-47}$ days and $\tau(H\alpha) = 127 \pm 18$ days, both too long to be measurable from our data. However, due to the lower sampling rate of the Hα light curve the ICCF analysis displays two possible peaks also at $\tau(H\alpha) \simeq 24$ days and $\tau(H\alpha) \simeq 151$ days, respectively.

Those results are inconsistent with the delays which were reported by Dietrich et al. (1998) using the data of the X-ray–UV–optical monitoring campaign in 1994/1995 (Leighly et al. 1997; O'Brien et al. 1998; Dietrich et al. 1998), i.e., $\tau(H\beta) = 23 \pm 4$ days and $\tau(H\alpha) = 19 \pm 9$ days and also with the results of this study (Table 6). However, the time delays which we determined for 3C 390.3 in 1995 are consistent with the delays we find for Hα and Hβ in this study. In 1995, the strength of the optical continuum corrected for host-galaxy contributions was $F_\lambda(5100$ Å$) = 1.16 \times 10^{-15}$ erg s^{-1} cm^{-2} Å^{-1}. During the 2005 monitoring campaign, the continuum was about ∼6× stronger (Table 5). Using the radius–luminosity relation for AGNs (Bentz et al. 2009a), it can be expected that the derived delays of the Hα and Hβ emission lines should be about ∼2.5× as long than those of 1995. This is in good agreement with the delays which we have measured (Table 6).
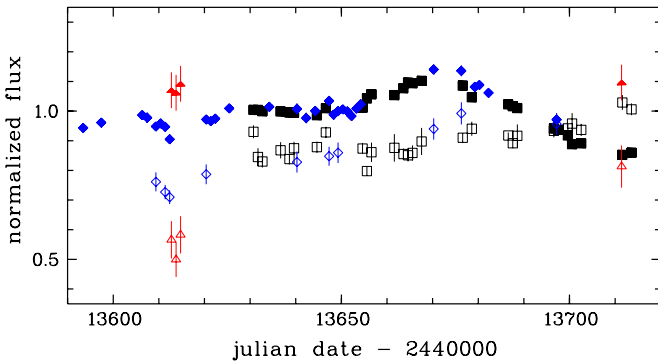
Figure 18. Comparison of the normalized light curves of the AGN continuum and of the broad Hβ emission-line flux of this study (black boxes), of Sergeev et al. (2002, 2011, blue diamonds), and of Shapovalova et al. (2010, red triangles). The continuum is shown as filled symbols and the Hβ emission-line flux is shown as open symbols. For better comparison the normalized light curves have been offset.

(A color version of this figure is available in the online journal.)

To investigate the cause of the discrepancy between the results based on the analysis of the variations over about 10 years compared with those covering about three months up to one year, we re-analyzed the data published by Sergeev et al. (2002, 2011) and Shapovalova et al. (2010). Using the data of the Sergeev et al. study, we compiled Hβ and F_λ(5100 Å) continuum light curves which cover about 15 years with 413 epochs for the continuum and 131 epochs for Hβ. We applied the same ICCF analysis to these light curves as we did for the measurements for this study. We found τ(Hβ) = $81.6^{+16.4}_{-22.5}$ days which is consistent with the results of Sergeev et al. and due to the large uncertainties, within 1σ it is even in the range with the result of this study. Next, we studied parts of the light curve which covered approximately 1000 days to study the impact of the luminosity state of 3C 390.3 on the delay. We found delays of the broad Hβ variations ranging from τ(Hβ) = 13^{+34}_{-30} days to τ(Hβ) = 102^{+11}_{-16} days with no clear relation between the continuum state and the delay. However, the mean spacing, especially for the Hβ emission-line flux measurements, is only $\sim$20 days to $\sim$160 days, i.e., probably not sufficient. Only for the last three years of the light curve the temporal sampling is about $\sim$6 days for the continuum and $\sim$20 days for the Hβ emission-line flux. For this period we find a delay of τ(Hβ) = 102^{+6}_{-6} days. The Hβ emission-line flux measurements by Sergeev et al. (2011) and by Shapovalova et al. (2010) do overlap with our monitoring campaign. Therefore, we can compare those with our Hβ emission-line light curve (Figure 18). It can be seen that the continuum light curve follows the variations we measured while the coverage in Hβ is not as high.

In the same way, we re-analyzed the continuum and Hβ emission-line light curves given by Shapovalova et al. (2010). For the entire data set, which covers about 12.5 years, we find τ(Hβ) = $96.2^{+35.4}_{-35.2}$ days, consistent with the results of Sergeev et al. Similar to the Sergeev et al. data the light curves were split up into periods of about 1000 days duration with temporal sampling of about 40 days. We found delays of the broad Hβ variations ranging from τ(Hβ) = 16^{+39}_{-41} days to τ(Hβ) = 210^{+55}_{-140} days with no clear relation between the continuum state and the delay.

In a study on the reliability of cross-correlation function time delay determinations Welsh (1999) has pointed out that variations on longer timescales, e.g., on the dynamical timescale of the BLR which is of the order of years, will shift the response

time to longer delays. Long-term variations are different from direct reverberation signals which measure the instantaneous response of the emission-line gas to continuum variations, while long-term variations trace a more gradual response to an overall increase or decrease of the continuum strength. To correct for this effect it is necessary to detrend light curves from those gradual changes. To detrend the continuum and Hβ emission-line variations, we fit a low order polynomial to the light curves. Next, we applied the analog time series analysis to the detrended light curves of the Sergeev et al. (2002, 2011) and Shapovalova et al. (2010) studies. We derived time delays of the Hβ variations of τ(Hβ) = $90.4^{+8.9}_{-9.2}$ days (Sergeev et al.) and τ(Hβ) = $82.7^{+13.9}_{-12.9}$ days (Shapovalova et al.). Within the uncertainties (1σ errors) these delays are consistent with those obtained with the original light curves. However, the uncertainties of the time delays using the detrented light curves are about a factor 2–3 smaller than those for the light curves including gradual long-term variations.

Furthermore, the properties of continuum strength variations have a significant effect on the time delay measured from cross-correlation functions. This issue can be responsible for the different delays measured in our study and those using variations of the continuum and the broad emission lines over more than 10 years, in particular, the auto-correlation function of the continuum, ACF$_{cont}$. It has been already noted by Sergeev et al. (2002, 2011) that the width of the ACF$_{cont}$ of the continuum light curve which is covering several years up to more than a decade is much broader than the ACF$_{cont}$ of a shorter campaign like the one in 1994/1995 and that this will result in a longer time delay (see also the Appendix for a more detailed discussion).

In addition, our campaign covered only a little more than 80 days and hence we are not able to measure time delays of about 100 days and more. We think that the different time delays are caused by the long time period of about a decade to cover the variation of 3C 390.3 and the wider temporal sampling of the measurements. Furthermore, the significantly different widths of the ACF$_{cont}$ and the fact that in addition to reverberation signals, i.e., the direct response of line-emitting gas to continuum variations, also variations of the emission-line flux are included. These are associated with changes of the physical conditions and the distribution of the gas which happen on dynamical timescales and which are uncorrelated with continuum variability also contributes to the different time delays. Therefore, a long duration campaign for 3C 390.3 with densely sampled measurements will be necessary to find a definitive result.

5.2. Black Hole Mass Estimates

A wide range of mass estimates for the SMBH of 3C 390.3 have been reported, ranging from $\sim$1.3 × 10^8 $M_\odot$ up to $\sim$7 × 10^9 $M_\odot$ using emission-line profile properties and estimates of the size of the BLR (e.g., Barr et al. 1980; Bentz et al. 2009b; Clavel & Wamsteker 1987; Gaskell 1996; Peterson et al. 2004; Sergeev et al. 2002, 2011; Wamsteker et al. 1997), as well as using the Ca II triplet in the near infrared employing the M–σ_* relation yielding about $M_{bh} \simeq$ 4 to 5 × 10^8 $M_\odot$ (Nelson et al. 2004). Most of these studies favor a black hole mass for 3C 390.3 of the order of 5 to 10 × 10^8 $M_\odot$. Our measurement of the mass of the black hole of 3C 390.3 with $M_{bh} = 0.86^{+0.19}_{-0.18} × 10^9 M_\odot$ (based on the separation of the blue and red peaks in the rms spectrum) and $M_{bh} = 1.26^{+0.21}_{-0.16} × 10^9 M_\odot$ (using σ_{line}) is consistent with the black hole mass based on the M–σ_* relation. Using the M–σ_* relation from Gültekin et al. (2009),

we calculated the stellar velocity dispersion σ_* which is expected for the host galaxy of 3C 390.3 based on our estimated black hole mass. We find $\sigma_* = 257^{+90}_{-70}$ km s^{-1} for 3C 390.3 which is consistent with $\sigma_* = 273 \pm 16$ km s^{-1} as measured by Nelson et al. (2004). Furthermore, simple disk models which we applied to describe the overall structure of the broad double-peaked hydrogen Balmer emission lines yield a mass estimate of $M_{\rm bh} \simeq 10^9\,M_\odot$.

An additional test for the reliability of the derived black hole mass for 3C 390.3 is given by the comparison of our measured values for the size and continuum luminosity of 3C 390.3 with the expected values derived from the radius–luminosity relation. Guided by simple photoionization models, a relation between the continuum luminosity of an AGN and the radius of the BLR is expected and Kaspi et al. (2000) provided the first convincing evidence for such a relation. Careful re-analysis and additional observations (e.g., Peterson et al. 2004; Bentz et al. 2006a, 2007, 2009b; Denney et al. 2006, 2009b, 2010; Grier et al. 2008; Onken et al. 2003) have reduced the uncertainty of the slope of the relation. It turned out that the correction for host galaxy contamination has a profound impact on the R–L relation (Bentz et al. 2006b, 2009a). With a slope of $\alpha = 0.52 \pm 0.04$ (Bentz et al. 2009a), we estimated the black hole mass of 3C 390.3. For the continuum flux at $\lambda = 5100$ Å, we used the average continuum flux of the AGN continuum (Table 5), corrected for host galaxy contributions, with $\lambda L_\lambda(5100\,\text{Å}) = 2.28 \times 10^{44}$ erg s^{-1} and the measured delay for the Hβ emission line is $\tau_{\rm cent} \simeq 44$ days. Using the radius–luminosity relation as given in Bentz et al. (2009a)

$$\log R_{\rm BLR} = K + \alpha \, \log\left(\lambda\, F_\lambda(5100\,\text{Å})\right) \qquad (5)$$

with $K = -21.3^{+2.9}_{-2.8}$ and $\alpha = 0.519^{+0.063}_{-0.066}$, the H$\beta$ BLR radius amounts to $\tau = 52.7^{+2.9}_{-2.8}$ days, which given the intrinsic scatter in the relationship, is consistent with the measured $\tau_{\rm cent}({\rm H}\beta) = 44.3^{+3.0}_{-3.3}$ days or the $\tau_{\rm cent}({\rm H}\beta) = 47.9^{+2.4}_{-4.2}$ days using SPEAR.

6. SUMMARY

We present results of a ground-based monitoring campaign on the BLRG 3C 390.3. Optical spectra and g-band imaging were obtained in late 2005 for three months using the 2.4 m telescope at MDM Observatory. Integrated emission-line flux variations were measured for the Balmer lines Hα, Hβ, Hγ, and for the helium line He IIλ4686, as well as g-band fluxes and the optical AGN continuum at 5100 Å. The g-band fluxes and the optical AGN continuum are varying simultaneously within the uncertainties ($\tau_{\rm cent} = -0.2 \pm 1.1$ days). We measure time delays for the emission-line variations with respect to the variable g-band continuum of $\tau({\rm H}\alpha) = 56.3^{+2.4}_{-6.6}$ days, $\tau({\rm H}\beta) = 44.3^{+3.0}_{-3.3}$ days, $\tau({\rm H}\gamma) = 58.1^{+4.3}_{-6.1}$ days, and $\tau({\rm He\ II}\ 4686) = 22.3^{+6.5}_{-3.8}$ days. The blue and red peaks in the double-peaked line profiles, as well as the blue and red outer profile wings, vary simultaneously within ± 3 days. This provides strong support for gravitationally bound orbital motion for the dominant part of the line-emitting gas. Using the separation of the blue and red peaks in the broad double-peaked profiles in the rms spectra of the Balmer emission lines and the corresponding time delays we determine a virial black hole mass of $M_{\rm bh}^{\rm vir} = 1.77^{+0.29}_{-0.31} \times 10^8\,M_\odot$ for the black hole of 3C 390.3. Using the inclination angle $i = 27° \pm 2°$ of the line-emitting region the intrinsic velocity, $v_{\rm intr}$, can be recovered from the measured $v_{\rm obs} = v_{\rm intr} \sin i$. This

results in a black hole mass of $M_{\rm bh} = (0.86^{+0.19}_{-0.18}) \times 10^9\,M_\odot$ for 3C 390.3 and $M_{\rm bh} = (1.26^{+0.21}_{-0.16}) \times 10^9\,M_\odot$ based on the $\sigma_{\rm line}$ of the rms spectrum. This mass estimate is consistent with the mass indicated by simple accretion disk models to describe the observed double-peaked profiles as well as with black hole masses derived from studies on the stellar dynamics of 3C 390.3. Furthermore, the mean continuum luminosity and the measured time delay for the broad emission-line flux variations of Hβ is consistent with the most recent AGN radius–luminosity relation. Thus, 3C 390.3 as a radio-loud AGN with a low Eddington ratio of only $L_{\rm edd}/L_{\rm bol} = 0.02$ follows the same AGN radius–luminosity relation as radio-quiet AGNs.

APPENDIX

AUTO-CORRELATION FUNCTION AND TIME DELAY

Under the assumption that the observed emission-line flux $L(t)$ is the superposition of the response of the emission-line gas to continuum variations $C(t)$ of gas with the same time delay, which are related by the transfer function $\psi(t)$, the measured emission-line flux can be written as

$$L(t) = \int_{-\infty}^{\infty} \psi(\tau)\, C(t - \tau)\, d\tau. \qquad (A1)$$

This equation can be also written using the CCF(t), ACF$_{\rm cont}$(t) and the transfer function $\psi(t)$ in the form

$$\text{CCF}(t) = \int_{-\infty}^{\infty} \psi(\tau)\, \text{ACF}_{\rm cont}(t - \tau)\, d\tau \qquad (A2)$$

as has been shown by Penston (1991), Koratkar & Gaskell (1991), and Peterson (1993, 2000). Hence, the measured time delay depends on both the ACF$_{\rm cont}$ of the AGN continuum and the transfer function $\psi(t)$. While the width of the ACF$_{\rm cont}$ at the FWHM of the continuum variations studied by Sergeev et al. (2002, 2011) and Shapovalova et al. (2010) amounts to about FWHM $\simeq$ 1600–2000 days, the FWHM of the continuum ACF in our 2005 monitoring campaign is FWHM (ACF$_{\rm cont}$) $\simeq$ 27 days, i.e., about $\sim$60 to $\sim$75 times narrower. In the context of investigating the impact of variations on longer timescales and the necessity of detrending light curves for those trends to recover the time delay, Welsh (1999) mentioned that the points in the ACF and CCF are highly correlated (e.g., Jenkins & Watts 1969) and that those correlations result in spurious large values of the CCF, especially for light curves that are characterized by intrinsically broad peaks. We suspect that the different time delays are predominantly caused by the significantly different widths of the ACF$_{\rm cont}$ (cf. Section 5.1).

In addition, using the variations of the broad emission-line flux over times scales of the order of the dynamical time will include not only variations which are directly associated with continuum variations, i.e., pure reverberation events, but will also include variations caused by changes in the distribution and conditions of the line-emitting gas. Those variations are manifested, for example, in emission-line profile changes which are uncorrelated with continuum variability, as shown by

Wanders & Peterson (1996). Hence, including emission-line profile variability will dilute a reverberation signal, i.e., the direct response of the gas on continuum variations. This aspect needs to be addressed when studying the relation of continuum and emission-line variability over timescales which are comparable or even longer than the dynamical timescale for an AGN.

Based on the variability of NGC 5548 which has currently the best covered spectroscopically variability history for the optical continuum and the broad Hβ emission-line flux, it has been shown that the measured time delay is strongly correlated with the strength of the continuum, i.e., whether the AGN is in a high or low state. Depending on the continuum luminosity, the delay of the Hβ flux response to continuum variations varies between $\tau(H\beta) = 4.2$ days and $\tau(H\beta) = 26.4$ days (Bentz et al. 2009b; Peterson et al. 2002). The continuum strength in the 13 years which were investigated in these studies varied by a factor of about $\sim$10. The light curves which were studied by Sergeev et al. (2002, 2011) and Shapovalova et al. (2010) cover more than 10 years. During this time the strength of the continuum of 3C 390.3 varied by a factor of nearly $\sim$6.

Finally, Horne et al. (2004) have studied the impact of the duration of a monitoring campaign on the measured time delay. They provide a guide line for the optimal length of monitoring campaign depending on the brightness of an AGN to also optimize the use of telescope time. They found that a campaign should last at least about three times the light crossing time of the BLR to recover the velocity resolved transfer function $\psi(\tau, v)$. In the case of cross-correlation functions, shorter campaigns can still yield reliable time delays, in particular if the light curve displays features of increasing and decreasing continuum and emission-line flux and not only a monotonic increase or decrease of the continuum and emission-line flux strength.

REFERENCES

Alef, W., Goetz, M. M. A., Preuss, E., & Kellermann, K. I. 1988, A&A, 192, 53
Alef, W., Preuss, E., Kellermann, K. I., Wu, S. Y., & Qui, Y. H. 1994, in Compact Extragalactic Radio Sources, Proc. NRAO Workshop, Socorro, New Mexico, ed. J. A. Zensus & K. I. Kellermann (Green Bank, WV: National Radio Astronomy Observatory (NRAO)), 55
Barr, P., Pollard, G., Sanford, P. W., et al. 1980, MNRAS, 193, 549
Baum, S. A., Heckman, T., Bridle, A., van Breugel, W., & Miley, G. 1988, ApJS, 68, 643
Bentz, M. C., Denney, K. D., Cackett, E. M., et al. 2006a, ApJ, 651, 775
Bentz, M. C., Denney, K. D., Cackett, E. M., et al. 2007, ApJ, 662, 205
Bentz, M. C., Horne, K., Barth, A. J., et al. 2010a, ApJ, 720, L46
Bentz, M. C., Peterson, B. M., Pogge, R. W., Vestergaard, M., & Onken, C. A. 2006b, ApJ, 644, 133
Bentz, M. C., Peterson, B. M., Netzer, H., Pogge, R. W., & Vestergaard, M. 2009a, ApJ, 697, 160
Bentz, M. C., Walsh, J. L., Barth, A. J., et al. 2009b, ApJ, 705, 199
Bentz, M. C., Walsh, J. L., Barth, A. J., et al. 2010b, ApJ, 716, 993
Bilir, S., Ak, S., Karaali, S., et al. 2008, MNRAS, 384, 1178
Blandford, R. D., & McKee, C. F. 1982, ApJ, 255, 419
Boroson, T. A. 2002, ApJ, 565, 78
Boroson, T. A., & Green, R. F. 1992, ApJS, 80, 109
Bromm, V., & Loeb, A. 2003, ApJ, 596, 34
Burbidge, M. E., & Burbidge, G. R. 1971, ApJ, 163, L21
Cannon, R. D., Penston, M. V., & Penston, M. J. 1968, Nature, 217, 340
Clavel, J., Reichert, G. A., Alloin, D., et al. 1991, ApJ, 366, 64
Clavel, J., & Wamsteker, W. 1987, ApJ, 320, L9
Collier, S., Horne, K., Kaspi, S., et al. 1998, ApJ, 500, 162
Collin, S., Kawaguchi, T., Peterson, B. M., & Vestergaard, M. 2006, A&A, 456, 75
Crenshaw, D. M., Kraemer, S. B., Bruhweiler, F. C., & Ruiz, J. R. 2001, ApJ, 555, 633
Davenport, J. R. A., Bochanski, J. J., Covey, K. R., et al. 2007, AJ, 134, 2430
Davidson, K., & Netzer, H. 1979, Rev. Mod. Phys., 51, 715
Denney, K. D., Bentz, M. C., Peterson, B. M., et al. 2006, ApJ, 653, 152
Denney, K. D., Peterson, B. M., Pogge, R. W., et al. 2009a, ApJ, 704, L80

Denney, K. D., Peterson, B. M., Pogge, R. W., et al. 2010, ApJ, 721, 715
Denney, K. D., Watson, L. C., Peterson, B. M., et al. 2009b, ApJ, 702, 1353
Dietrich, M., Appenzeller, I., Vestergaard, M., & Wagner, S. J. 2002, ApJ, 564, 581
Dietrich, M., Crenshaw, D. M., & Kraemer, S. B. 2005, ApJ, 623, 700
Dietrich, M., Hamann, F., Appenzeller, I., & Vestergaard, M. 2003, ApJ, 596, 817
Dietrich, M., Kollatschny, W., Peterson, B. M., et al. 1993, ApJ, 408, 416
Dietrich, M., Mathur, S., Grupe, D., & Komossa, S. 2009, ApJ, 696, 1998
Dietrich, M., Peterson, B. M., Albrecht, P., et al. 1998, ApJS, 115, 185
Di Matteo, T., Croft, R. A., Springel, V., & Hernquist, L. 2004, ApJ, 610, 80
Elvis, M., Belinda, J., McDowell, J. C., et al. 1994, ApJS, 95, 1
Eracleous, M., & Halpern, J. P. 1994, ApJS, 90, 1
Eracleous, M., & Halpern, J. P. 2003, ApJ, 599, 886
Eracleous, M., Halpern, J. P., & Livio, M. 1996, ApJ, 459, 89
Ferrarese, L., Pogge, R. W., Peterson, B. M., et al. 2001, ApJ, 555, L79
Flohic, H. M. L. G., & Eracleous, M. 2008, ApJ, 686, 138
Fukugita, M., Ichikawa, T., Gunn, J. E., et al. 1996, AJ, 111, 1748
Gaskell, C. M. 1996, ApJ, 464, L107
Gaskell, C. M., & Ferland, G. J. 1984, PASP, 96, 393
Gaskell, C. M., & Peterson, B. M. 1987, ApJS, 65, 1
Gebhardt, K., Kormendy, J., Ho, L. C., et al. 2000, ApJ, 543, L5
Gezari, S., Halpern, J. P., & Eracleous, M. 2007, ApJS, 169, 167
Grier, C. J., Peterson, B. M., Bentz, M. C., et al. 2008, ApJ, 688, 837
Grier, C. J., Peterson, B. M., Pogge, R. W., et al. 2012, ApJL, 744, L4
Gültekin, K., Richstone, D. O., Gebhardt, K., et al. 2009, ApJ, 698, 198
Gültekin, K., Tremaine, S., Loeb, A., & Richstone, D. O. 2011, ApJ, 738, 17
Haiman, Z., & Loeb, A. 1998, ApJ, 503, 505
Haiman, Z., & Loeb, A. 2001, ApJ, 552, 459
Halpern, J. P., & Steiner, J. E. 1983, ApJ, 269, L37
Horne, K., Peterson, B. M., Collier, S. J., & Netzer, H. 2004, PASP, 116, 465
Jenkins, G. M., & Watts, D. G. 1969, Spectral Analysis and its Applications (San Francisco, CA: Holden-Day)
Jovanovic, P., Popovic, L. C., Stalevski, M., & Shapovalova, A. I. 2010, ApJ, 718, 168
Kaspi, S., Smith, P. S., Netzer, H., et al. 2000, ApJ, 533, 631
Kelly, B. C., Bechtold, J., & Siemiginowska, A. 2009, ApJ, 698, 895
Kinney, A. L., Calzetti, D., Bohlin, R. C., et al. 1996, ApJ, 467, 38
Kollatschny, W. 2003, A&A, 407, 461
Koratkar, A. P., & Gaskell, C. M. 1991, ApJS, 75, 719
Korista, K. T., Alloin, D., Barr, P., et al. 1995, ApJS, 97, 285
Korista, K. T., & Goad, M. R. 2001, ApJ, 553, 695
Kozłowski, S., Kochanek, C. S., Udalski, A., et al. 2010, ApJ, 708, 927
Laor, A. 2000, ApJ, 543, L111
Leahy, J. P., & Perley, R. A. 1995, MNRAS, 277, 1097
Leighly, K. M., O'Brien, P. T., Edelson, R., et al. 1997, ApJ, 483, 767
Lewis, K. T., & Eracleous, M. 2006, ApJ, 642, 711
Lynds, R. C. 1968, AJ, 73, 888
MacLeod, C. L., Ivezić, Ž., Kochanek, C. S., et al. 2010, ApJ, 721, 1014
Marconi, A., Axon, D. J., Maiolino, R., et al. 2008, ApJ, 678, 693
Merritt, D., & Ferrarese, L. 2001, ApJ, 547, 140
Morgan, C. W., Byard, P. L., DePoy, D. L., et al. 2005, AJ, 129, 2504
Mushotzky, R. F., Edelson, R., Baumgartner, W., & Gandhi, P. 2011, ApJ, 743, L12
Nelson, C. H., Green, R. F., Bower, G., Gebhardt, K., & Weistrop, D. 2004, ApJ, 615, 652
Netzer, H. 1982, MNRAS, 198, 589
Netzer, H. 2003, ApJ, 583, L5
Netzer, H., & Peterson, B. M. 1997, in Astronomical Time Series, ed. D. Maoz, A. Sternberg, & E. M. Leibowitz (Dordrecht: Kluwer), 85
O'Brien, P. T., Dietrich, M., Leighly, K., et al. 1998, ApJ, 509, 163
Onken, C. A., Ferrarese, L., Merritt, D., et al. 2004, ApJ, 615, 645
Onken, C. A., & Peterson, B. M. 2002, ApJ, 572, 746
Onken, C. A., Peterson, B. M., Dietrich, M., Robinson, A., & Salamanka, I. M. 2003, ApJ, 585, 121
Osterbrock, D. E., & Ferland, G. 2005, Astrophysics of Gaseous Nebulae and AGN (Mill Valley, CA: Univ. Science Books)
Osterbrock, D. E., Koski, A. T., & Phillips, M. M. 1976, ApJ, 206, 898
Penston, M. J., Penston, M. V., & Sandage, A. 1971, PASP, 83, 783
Penston, M. V. 1991, in Variability of Active Galactic Nuclei, ed. H. R. Miller & P. J. Wiita (Cambridge: Cambridge Univ. Press), 343
Penston, M. V., & Perez, E. 1984, MNRAS, 211, 33
Peterson, B. M. 1993, PASP, 105, 247
Peterson, B. M. 2000, in Advanced Lectures on The Starburst—AGN Connection, ed. I. Aretxaga, D. Kunth, & R. Mujica (Singapore: World Scientific), 36

Peterson, B. M. 2003, in ASP Conf. Ser. 290, Active Galactic Nuclei: from Central Engine to Host Galaxy, ed. S. Collin, F. Combes, & I. Shlosman (San Francisco, CA: ASP), 43
Peterson, B. M., Balonek, T. J., Barker, E. S., et al. 1991, ApJ, 368, 119
Peterson, B. M., Berlind, P., Bertram, R., et al. 2002, ApJ, 581, 197
Peterson, B. M., Ferrarese, L., Gilbert, K. M., et al. 2004, ApJ, 613, 682
Peterson, B. M., & Wandel, A. 1999, ApJ, 521, L95
Peterson, B. M., & Wandel, A. 2000, ApJ, 540, L13
Peterson, B. M., Wanders, I., Horne, K., et al. 1998, PASP, 110, 660
Popovic, L. C., Shapovalova, A. I., Ilić, D., et al. 2011, A&A, 528, 130
Press, W. H., Teukolsky, S. A., Vetterling, W. T., & Flannery, B. P. 1992, Numerical Recipes in FORTRAN. The Art of Scientific Computing (Cambridge: Cambridge Univ. Press)
Reichert, G. A., Rodriguez-Pascual, P. M., Alloin, D., et al. 1994, ApJ, 425, 582
Richards, G. T., Lacy, M., Storrie-Lombardi, L. J., et al. 2006, ApJS, 166, 470
Rodriguez-Pascual, P. M., Alloin, D., Clavel, J., et al. 1997, ApJS, 110, 9
Rybicki, G. B., & Press, W. H. 1992, ApJ, 398, 169
Sandage, A. 1966, ApJ, 145, 1
Santos-Lleó, M., Chatzichristou, E., Mendes de Oliveira, C., et al. 1997, ApJS, 112, 271
Schlegel, D. J., Finkbeiner, D. P., & Davis, M. 1998, ApJ, 500, 525
Seaton, M. J. 1979, MNRAS, 187, 73P
Selmes, R. A., Tritton, K. P., & Wordsworth, R. W. 1975, MNRAS, 170, 15
Sergeev, S. G., Klimanov, S. A., Doroshenko, V. T., et al. 2011, MNRAS, 410, 1877
Sergeev, S. G., Pronik, V. I., Peterson, B. M., Sergeeva, E. A., & Zheng, W. 2002, ApJ, 576, 660
Shapovalova, A. I., Popović, L. Č., Burenkov, A. N., et al. 2010, A&A, 517, A42
Shen, B. S. P., Usher, P. D., & Barrett, J. W. 1972, ApJ, 171, 457
Silk, J., & Rees, M. J. 1998, A&A, 331, L1

Smith, J. A., Allam, S. S., Tucker, D. L., & Fornal, B. 2007, BAAS, 39, 964
Smith, J. A., Tucker, D. L., Kent, S., et al. 2002, AJ, 123, 2121
Stirpe, G. M., Winge, C., Altieri, B., et al. 1994, ApJ, 425, 609
Tao, J., Fan, J., Qian, B., & Liu, Y. 2008, AJ, 135, 737
Tremaine, S., Gebhardt, K., Bender, R., et al. 2002, ApJ, 574, 740
Tucker, D. L., Kent, S., Richmond, M. W., et al. 2006, Astron. Nachr., 327, 821
van Groningen, E., & Wanders, I. 1992, PASP, 104, 700
Veilleux, S., & Zheng, W. 1991, ApJ, 377, 89
Véron-Cetty, M.-P., Joly, M., & Véron, P. 2004, A&A, 417, 515
Vestergaard, M. 2004, ApJ, 601, 676
Volonteri, M., & Begelman, M. C. 2010, MNRAS, 409, 1022
Volonteri, M., & Rees, M. J. 2006, ApJ, 650, 669
Walsh, J. L., Minezaki, T., Bentz, M. C., et al. 2009, ApJS, 185, 156
Wamsteker, W., Tang-gui, W., Schartel, N., & Vio, R. 1997, MNRAS, 288, 225
Wanders, I., & Peterson, B. M. 1996, ApJ, 466, 174
Wanders, I., Peterson, B. M., Alloin, D., et al. 1997, ApJS, 113, 69
Welsh, W. F. 1999, PASP, 111, 1347
White, J. R., & Peterson, B. M. 1994, PASP, 106, 879
Whittle, M. 1985a, MNRAS, 213, 1
Whittle, M. 1985b, MNRAS, 213, 33
Whittle, M. 1985c, MNRAS, 216, 817
Wills, B. J., Netzer, H., & Wills, D. 1985, ApJ, 288, 94
Woo, J.-H., Treu, T., Barth, A. J., et al. 2010, ApJ, 716, 269
Wyndham, J. D. 1966, ApJ, 14, 459
Yee, H. K. C., & Oke, J. B. 1981, ApJ, 248, 472
Yoo, J., & Miralda-Escudé, J. 2004, ApJ, 614, L25
Zheng, W. 1996, AJ, 111, 1498
Zheng, W., Perez, E., Grandi, S. A., & Penston, M. V. 1995, AJ, 109, 2355
Zu, Y., Kochanek, C. S., Kozłowski, S., & Udalski, A. 2012, ApJ, submitted (arXiv:1202.3782.v1)
Zu, Y., Kochanek, C. S., & Peterson, B. M. 2011, ApJ, 735, 80